Carbon dioxide in geochemically heterogeneous melt inclusions from Mount Etna, Italy

L. C. Salem[1], M. Edmonds[1*], R. A. Corsaro[2], J. Maclennan[1]

[1]Department of Earth Sciences, University of Cambridge, Downing Street, Cambridge, CB2 3EQ, United Kingdom

[2]Istituto Nazionale di Geofisica e Vulcanologia, Sezione di Catania, Osservatorio Etneo, Piazza Roma 2, 95123 Catania, Italy

*corresponding author: marieedmonds@esc.cam.ac.uk

Key points:

- Melt inclusion geochemistry indicates that the melts supplying Mt. Etna are heterogeneous with respect to trace and volatile elements.
- Melts may be influenced by crustal carbonate assimilation, or by recycled plagioclase-rich cumulates in the mantle.
- Rapidly rising melts at Etna may become supersaturated in volatiles, causing a burst of shallow degassing, which may trigger eruptions.

Abstract

Mt. Etna is among the largest global volcanic outgassers with respect to carbon and sulfur, yet questions remain regarding the source of these volatiles and their systematics in the crust and mantle. The importance of heterogeneous mantle sources, mixing, crustal assimilation and disequilibrium degassing are investigated using melt inclusions erupted during the A.D. 1669 eruption of Mt. Etna, Italy. We find that the melt inclusion compositions define a mixing array between two geochemically distinct melts. One end-member melt is depleted in light rare Earth elements (LREE) and enriched in strontium (Sr), carbon and sulfur; the other is enriched in LREE and depleted in Sr, carbon and sulfur. We infer, through modeling, that the melts may either have been generated by melting a mantle source that includes a recycled oceanic crustal component; or they may have assimilated carbonate material in the crust. The resulting LREE-depleted, Sr-enriched melts were also alkali-rich, which enhanced the

solubility of carbon and sulfur. The LREE-depleted, Sr- and volatile-rich melt ascended through the crust and likely became supersaturated with respect to CO_2 and sulfur. The melt intruded into a LREE-enriched, relatively degassed magma body in the shallow crust, cooled rapidly and vesiculated, likely triggering eruption. The melt inclusion array trapped by growing olivines during this intrusion process records a snapshot of incomplete mixing between the two melts. Mt. Etna is renowned for the large increases in CO_2 gas fluxes shortly before and during eruption. The intrusion of supersaturated, CO_2-enhanced magmas into shallow reservoirs may be a common process at Mt. Etna.

1 Introduction

Mt. Etna, Italy, is one of the most prolific volcanic outgassers [*Aiuppa et al.*, 2006; *Allard et al.*, 1991; *Gerlach*, 1991; *Halmer et al.*, 2002], supplying almost 10% of the global volcanic output of carbon dioxide (CO_2) annually [*Burton et al.*, 2013]. Explosive eruptions of Mt. Etna over the past decade have been preceded by increases in the CO_2 gas flux from the volcano, perhaps caused by the migration of CO_2-rich exsolved fluids ahead of the ascending magma [*Aiuppa et al.*, 2006; *Aiuppa et al.*, 2007]. Melt inclusion studies have shown that CO_2-rich fluids may segregate at deep levels and flush melts stored in shallow reservoirs [*Andronico and Corsaro*, 2011; *Collins et al.*, 2009; *Métrich et al.*, 2004; *Spilliaert et al.*, 2006b]. The water (H_2O) and CO_2 content of melt inclusions has been used - assuming the melts are vapor-saturated and have degassed in equilibrium - to estimate pressures of melt inclusion entrapment of 150 to 400 MPa [*Corsaro et al.*, 2014; *Spilliaert et al.*, 2006a; *Spilliaert et al.*, 2006b]. The large scatter in the CO_2 concentrations, which deviate greatly from equilibrium closed system degassing paths (in common with many melt inclusion volatile datasets) [*Métrich and Wallace*, 2008], has been ascribed to a wide range of processes including gas fluxing, mixing and post-entrapment processes [*Bucholz et al.*, 2013; *Gaetani et al.*, 2012; *Hartley et al.*, 2014; *Maclennan*, 2017; *Sides et al.*, 2014; *Wallace et al.*, 2015]. The origin of the carbon has been debated. Its isotopic composition, expressed as C, ranges from -4.5 to -1.0 per mil [*Allard et al.*, 1991; *Chiodini et al.*, 2010]. This isotopic composition suggests either a heterogeneous and relatively heavy carbon reservoir in the mantle, that was recycled during subduction [*Frezzotti et al.*, 2009], or a mixture between MORB-like mantle carbon and a heavier crustal limestone component [*Chiodini et al.*, 2010; *Marziano et al.*, 2008; *Mason et al.*, 2017; *Mollo et al.*, 2010]. The trace element compositions of primitive melt inclusions suggest that the melts supplying Mt. Etna are heterogeneous, implying not only different degrees of melting, but also a highly enriched

mantle source that was influenced by subduction fluids [*Correale et al.*, 2014; *Kamenetsky et al.*, 2007; *Schiavi et al.*, 2015; *Viccaro and Cristofolini*, 2008].

In this study, the geochemistry of melt inclusions in tephra produced by the historic A.D. 1669 eruption are examined. This eruption was the largest of the past 500 years at Mt. Etna [*Branca and Ferrara*, 2013; *Corsaro et al.*, 1996] and one that marked a significant change in both the style of eruption and the composition of lavas [*Mulas et al.*, 2016]. A combination of micro-analytical techniques are used to constrain the major, trace and volatile element chemistry of melts trapped in olivine phenocrysts and to model processes that affect melt batches and fractionate their chemistry. In particular, we seek to deconvolve the different processes affecting the differentiation of the melt feeding the volcanic system at Mt. Etna, how CO_2 and sulfur concentrations vary with trace element compositions and consequently whether CO_2 is sourced from crustal carbonate or from the mantle. In doing so, the integrity of the melt inclusions is tested along with the assumption of equilibrium degassing of melts feeding Mt. Etna, Italy. These results have implications for the interpretation of pulses of CO_2 gas flux prior to eruptions [*Aiuppa et al.*, 2007].

2 Geological Setting

Mt. Etna (Sicily, Italy) is the largest active volcano in Europe and one of the most persistently active volcanoes globally (**Figure 1**). It is situated at the intersection of several major fault systems associated with the subduction of the African plate beneath the Eurasian plate [*Doglioni et al.*, 2001; *Gvirtzman and Nur*, 1999], yet its lavas are geochemically similar to ocean island basalts [*Montelli et al.*, 2006; *Schiano et al.*, 2001; *Schiavi et al.*, 2015; *Tanguy et al.*, 1997]. Melts originate in the asthenosphere [*Schiavi et al.*, 2015] and interact with thick lithospheric mantle [*Corsaro et al.*, 2014; *Marty et al.*, 1994] and carbonate- and cumulate-bearing crust [*Correale et al.*, 2014; *Corsaro et al.*, 2009]. Mt. Etna rests upon a subvolcanic sedimentary basement made of marls and clays, limestones and terrigeneous sedimentary rocks (~ 2 km thick) that form the Maghrebian–Appennine Chain [*Catalano et al.*, 2004]. These sediments overlie the Hyblean Plateau, a Mesozoic to Mid-Pleistocene carbonate succession of limestone and dolomite [*Pedley and Grasso*, 1992], which begins at a depth of ~5 km and has an average thickness of about 10 km and may interact thermally with rising magmas [*Heap et al.*, 2013]. Despite the occurrence of variably altered carbonate xenoliths, particularly in the lavas erupted in 1989 [*Michaud*, 1995], and

heavy carbon isotopes in volcanic gases that has been linked to carbonate assimilation [*Chiodini et al.*, 2011; *Mason et al.*, 2017], petrological and geochemical evidence for direct carbonate assimilation has been lacking.

Lavas erupted from Mongibello, the most recent (15 ka to present) volcanic edifice of the Etnean succession, belong to a mildly alkaline series and have compositions that are variable from trachybasalt to benmoreite [*Corsaro and Pompilio*, 2004] and references therein). Most products are sodic (hawaiites) but, since the 1970s, there has been a shift towards a more potassic affinity (K-trachybasalts), with varying degrees of K-enrichment. Petrological data and geophysical evidence suggest that Mt. Etna's plumbing system is complex. A highly porphyritic plagioclase-rich, K-trachybasalt is the most commonly-erupted magma during both summit and flank eruptions, ascending from a shallow storage region (<5 km b.s.l.). There is also infrequent eruption of nearly aphyric basaltic magma that may ascend directly from a deeper region (10-12 km b.s.l) of the plumbing system. In the last 50 years this magma has erupted in 1974 [*Bottari et al.*, 1975; *Corsaro et al.*, 2009; *Tanguy et al.*, 1997], 2001 [*Corsaro et al.*, 2007; *Métrich et al.*, 2004] and 2002-2003 [*Andronico et al.*, 2005; *Spilliaert et al.*, 2006b]. Geophysical evidence suggests that magma reservoirs exist at 1-5 km and 10-15 km depth where there are cumulates and dyke structures, as indicated by seismic high-velocity bodies [*Aloisi et al.*, 2002; *Hirn et al.*, 1991; *Patanè et al.*, 2006] and recent petrological studies [*Corsaro et al.*, 2014]. There is also evidence, for some eruptions, of deeper melt storage close to the Moho (e.g. from crystallization of pyroxene before plagioclase in the 1974 lavas) [*Tanguy and Kieffer*, 1977].

Mt. Etna is an important global source of volcanic gases rich in sulfur and carbon, with annual CO_2 fluxes of up to 6 x 10^9 kg per year [*Burton et al.*, 2013]. Much of this carbon outgassing flux occurs between eruptions [*Allard et al.*, 1991]. Previous melt inclusion studies have shown the melts contain at least 0.3 wt.% sulfur at 140 MPa (from H_2O-CO_2 barometry) and magmas are fluxed with CO_2-rich magmatic vapor [*Allard et al.*, 2006; *Collins et al.*, 2009; *Ferlito et al.*, 2008; *Spilliaert et al.*, 2006b]. The vapor may precede the transport of magma to the surface on a timescale from days to weeks [*Aiuppa et al.*, 2007; *Aiuppa et al.*, 2008].

The A.D. 1669 eruption, which began on 11th March and lasted for four months, was the

largest and most destructive in historical times, largely due to the relatively low elevation of the vents (the main scoria cone, Monti Rossi, is at 800 m a.s.l.; **Figure 1**), the large volume of lava erupted (607 ± 105 x 10^6 m) [*Branca et al.*, 2013] and the high average effusion rate of 58 m/s. The lava flowed 17 km from the vent, impacting a densely-populated area and partly destroying Catania (**Figure 1**) [*Branca et al.*, 2013]. Strombolian activity initially produced a large, 1 km wide and 200 m high, scoria cone (**Figure 1**) and a thick, widespread pyroclastic fall deposit along the lower south-east flank of the volcano [*Mulas et al.*, 2016]. The total tephra fall volume, including the Monti Rossi cone, is estimated to be 6.6 x 10 m (about 3.2 x 10 m dense rock equivalent (DRE)) [*Mulas et al.*, 2016]. Later, the eruption produced a wide 'a'a flow-field [*Branca and Vigliotti*, 2015; *Branca et al.*, 2013].

Lavas erupted early in the A.D. 1669 eruption (denoted 'SET1' by [*Corsaro et al.*, 1996]) are more primitive than those erupted during the later stages of the eruption ('SET2'). Throughout the eruption the bulk rock mean MgO content decreases from a mean of 6.65 wt.% to 5.07 wt.% [*Corsaro et al.*, 1996]. This change in bulk composition has been interpreted as evidence for fresh mafic magma intruding into a shallow reservoir containing more evolved magma [*Corsaro et al.*, 1996]. However, a more recent study of 1669 lavas has shown that lavas erupted before 29 March 1669 (i.e 'SET1') are geochemically similar to lavas erupted after 29 March 1669 (i.e. 'SET2'), and both are similar to the Monti Rossi scoria compositions reported by [*Mulas et al.*, 2016]. The significantly higher Al_2O_3, SiO_2 and total alkalis of the 'SET2' reported by [*Corsaro et al.*, 1996] are proposed to be due to plagioclase accumulation [*Kahl et al.*, 2017]. The Monti Rossi cone, which we sample and analyze here, was formed rapidly, largely over the first two days of the eruption: 11, 12 March 1669 [*Mulas et al.*, 2016] (equivalent to the 'SET1' of [*Corsaro et al.*, 1996; *Kahl et al.*, 2017]).

A study of core to rim olivine compositions from the SET1 and SET2 lavas demonstrated more complex syn- and pre-eruptive environments [*Kahl et al.*, 2017]. Olivine cores in the 'SET1' lavas (which are similar to the Monti Rossi tephras; [*Mulas et al.*, 2016]) have a composition of $Fo_{75–78}$, and are inferred to have formed in a partially degassed environment together with clinopyroxene (Mg# 81–83), plagioclase (An_{66-75}) and Fe–Ti oxides (Mt_{35-52}), at a temperature of ~1170 °C and pressures of <1 kbar [*Kahl et al.*, 2017]. The olivine cores define a compositional plateau formed under relatively uniform

conditions, whereas the olivine rims (Fo_{51-59}) define a broad compositional range that may form over a broad pressure range <1 kbar. The 'SET2' lavas, erupted later in the eruption (not studied in the current work) contain olivines with similar composition cores, and much less evolved rims (Fo_{65-69}). Three distinct magma reservoirs located in the volcano's shallow plumbing system and several events of magma recharge have been proposed, based on studies of these olivines, in the 1.5 years leading up to the eruption, with the SET1 and SET2 magmas being derived from a distinct, bifurcated feeding dyke system [*Kahl et al.*, 2017].

The A.D. 1669 eruption marked a significant change in the geochemical and eruptive regime of Mt. Etna [*Clocchiatti et al.*, 1988; *Condomines et al.*, 1995]. From A.D. 1600 to 1669, volcanic activity was frequent, long-lasting and of high-volume effusive eruptions of plagioclase-phyric lavas. In contrast, the period A.D. 1670-1750 was characterized by sporadic and shorter eruptions with low effusion rates and more mafic lavas. This eruption provides an opportunity to observe a large spectrum of geochemically diverse melts at a critical point in Mt. Etna's recent history and to understand how this melt heterogeneity maps on to volatile systematics.

3 Sampling and analytical techniques

Glassy tephra was sampled from two localities (north-east: NEMR and south-west: SWMR) at the base of the main scoria cone, Monti Rossi, in Nicolosi on the South-East flank of Mt. Etna (**Figure 1**), from the MR1 unit of Mulas et al. [*2016*]. The scoria cone was erupted over the first two days of the eruption [*Corsaro et al.*, 1996; *Kahl et al.*, 2017; *Mulas et al.*, 2016]. Melt inclusions with included oxide crystals were analyzed but showed no systematic trend in major or trace element concentration with oxide-free MIs (**Supplementary Figure 1**), suggesting they may be 'pre-entrapment' phases. Crystals were individually mounted in CrystalBond and polished to expose melt inclusions before being re-mounted in Buehler EpoThin resin and re-polished for analysis. The thirty-one melt inclusions analyzed in this study are without cracks or shrinkage bubbles (**Figure 2**). We note that avoiding melt inclusions with shrinkage bubbles may bias the dataset; it is possible we may miss an earlier population of melt inclusions, for example (i.e. prior to any pre-eruptive mixing).

Trace elements, F, H_2O and CO_2 were analyzed by Secondary Ion Mass Spectrometry (SIMS) using a Cameca ims-4f instrument at the NERC Ion Microprobe Facility at the

University of Edinburgh, UK. CO_2 analyses were performed first, with a high mass resolution configuration, in order to enable good separation of C and Mg peaks. H_2O, F and trace elements were then measured with a lower mass resolution configuration. Errors in CO_2 and H_2O were assessed using repeat analyses of a suite of basaltic glass standards [*Pichavant et al.*, 2009]. Precision for H_2O and CO_2 was 1%. Average accuracy, expressed as % recovery of published compositions determined by FTIR, was 100.6%. NIST-610 was used as the calibration standard for trace element analyses [*Jochum et al.*, 2011]. Accuracy was monitored by analysis of international standards, NIST-610 and BCR-2G throughout analytical sessions. The accuracy of published compositions, relative to NIST-610 and BCR-2G standards [*Jochum et al.*, 2005; *Jochum et al.*, 2011] (given by $|(100 - A)|$, where A is the % recovery (given by the unknown determination divided by the known values, expressed as a %) (**Table S1**) was <16% for all trace elements and <5% for most trace elements (**Table S1**). Precision was estimated as 1 standard deviation relative error and varied between 0.1% (Ce) and 15.8% (Eu) using repeat analyses of BCR-2G [*Jochum et al.*, 2011]. Precision was calculated for trace element ratios and volatile/trace ratios using repeat analyses of the same standards. 1 percentage relative error (in parentheses) was calculated for La/Yb (0.5), Ce/Y (2.9), CO/Nb (0.9) and HO/Ce (1.1).

Major elements, S and Cl were determined by electron probe microanalysis (EPMA) using a Cameca SX100 instrument at the Department of Earth Sciences at the University of Cambridge, UK. Full details of the analytical set-up for SIMS and EPMA and error analysis are detailed in the **Supplementary Material Table 1**.

Signal-to-noise ratios were calculated for all elements analyzed in order to assess the contribution of natural variation and analytical error to the generation of sample variability. The method described in [*Maclennan et al.*, 2003] was used:

$$\sigma_t^2 = \sigma_0^2 - \sigma_r^2$$

, where σ_t is the true variation of the sample set, σ_0 is the observed variation and σ_r is an estimate of analytical error. The χ^2 distribution was used to assess the quality of σ_r , which depends on the number of repeat analyses to estimate analytical precision, in order to test whether signal-to-noise ratios are significant at a given confidence level. Signal-to-noise

ratios for all major and trace elements in glass are greater than the threshold for significant variability at the 99% confidence interval. Signal-to-noise ratios are high for incompatible and abundant elements. For example, Sr has a signal-to-noise ratio of σ_t/σ_r = 11.5, whereas Nd, which is less abundant, has σ_t/σ_r = 2.2 and Nb, which is more incompatible has σ_t/σ_r = 4.8. Elements that were analyzed with low precision have low signal-to-noise ratios, such as Gd (σ_t/σ_r = 0.5), and it is not possible to resolve natural variability through analytical noise.

4 Results

4.1 Crystal assemblage

The crystallinity of the tephra samples was estimated to lie in the range 10 to 25 vol.% (consistent with the 'porphyricity' measured for the lava samples, which ranges from 21-30 vol% [*Kahl et al.*, 2017]), with olivine, plagioclase (which makes up 60-80 vol.% of the crystals), augite and titanomagnetite. This crystal assemblage is consistent with other recent studies of the 1669 eruption lava flows [*Corsaro et al.*, 1996; *Kahl et al.*, 2017]. Host core olivine compositions fall within a narrow range, $Fo_{73\text{-}76}$ (see **Supplementary Material**) overlapping the olivine compositions of the two dominant groups (Type IV and VII) of [*Kahl et al.*, 2017]. Matrix glass magnesium numbers (Mg#) range from 37 to 42. The olivine cores are in general too forsteritic to be in equilibrium with the carrier liquid using a K_d of ~0.30, where Kd is equal to $\left(X_{Fe^{2+}}/X_{Mg}\right)_{ol} \Big/ \left(X_{Fe^{2+}}/X_{Mg}\right)_{liq}$ [*Roeder and Emslie*, 1970] (**Supplementary Material Figure S6**).

4.2 Melt inclusion major element composition

Melt inclusion compositions may be modified by post-entrapment crystallization (PEC). The extent of PEC was estimated using Petrolog3 in reverse fractional crystallisation mode, which accounts for Fe-Mg diffusion between the host olivine and the melt inclusion [*Danyushevsky and Plechov*, 2011b] and it was found that all inclusions experienced 5-10% PEC. This affects the MgO and FeO of the melt inclusion and thus the Mg# is recalculated to 45-51 (shown in **Supplementary Table 5**). The Mg# was calculated for the matrix glass and melt inclusions using only Fe assuming that FeO is 0.70 to 0.85 Fe [*Metrich and Clocchiatti*, 1989] (**Supplementary Table 5**). The major element compositions of the melt inclusions are K-poor trachybasaltic, typical of pre-1970 lavas and similar to the plagioclase-rich and K-

poor products of the 1763 eruption [*Corsaro et al.*, 2009]. Major element oxide compositions are within the field for post-1500 Etnean lavas [*Corsaro et al.*, 1996; *Cristofolini and Romano*, 1982] and recent 21st century eruption melt inclusion analyses (**Figure 3**) [*Collins et al.*, 2009; *Métrich et al.*, 2004; *Schiavi et al.*, 2015; *Spilliaert et al.*, 2006b] but far more evolved than the olivine-hosted MI from the 4 kyr Fall Stratified eruption at Mt. Etna (hereafter FS) [*Kamenetsky et al.*, 2007], considered one of the most primitive melts erupted at Mt. Etna.

4.3 Melt inclusion trace element composition

The melt inclusions are relatively enriched in incompatible trace elements compared to N-MORB. The trace element patterns normalised to primitive mantle for melt inclusions and matrix glasses display greater enrichment in LREE and Nb than HREE (**Figure 4**). Concentrations of Nb in the 1669 melt inclusions range from 50 to 140 ppm, La 60-140 ppm, and Nd 50-100 ppm (**Figure 5a**), 2-3 times greater than the primitive FS MI measured by [*Kamenetsky et al.*, 2007] (**Figure 5**, coloured circles), but within the range of recent eruptions in 2001-2007 [*Collins et al.*, 2009; *Schiavi et al.*, 2015]. Ce/Y varies between 2 and 6 (**Figure 5b**) similar to the range in both the FS MI [*Kamenetsky et al.*, 2007] and 2001-2006 melt inclusions [*Schiavi et al.*, 2015]. A.D. 1669 matrix glass compositions also lie within this range (gray inverse triangles). The most enriched melt inclusions (with highest LREE/HREE ratios) are also those with the highest absolute concentrations of LREE (**Figure 5a**). The full suite of crystals host compositionally-variable melts with Ce/Y ratios between 2 and 6 which is independent of the host olivine composition for both the A.D. 1669 MI and FS (**Supplementary Figure 2**). It is worthy of note that the trace element diversity in the melt inlcusions far exceeds the diversity in whole rock compositions for the SET1 lavas, for which Ce/Y only varies by ~ 3% and K_2O only from 1.3 to 1.6 wt% [*Mulas et al., 2016*].

A correlation coefficient matrix reveals broad-scale correlation trends in the data (**Supplementary Figure 3**). Ba, La, Nb, Ce, Pr, Nd and Zr show strong positive correlations with each other ($r > 0.9$) but a weak negative correlation with HREE and Y ($r = -0.2$) suggesting that the primary melts were generated from sources with variable LREE-enrichment, or from variable degrees of fractional melting at a pressure where garnet is present to fractionate HREE from LREE. Sr shows a weak negative correlation with the LREE ($r = -0.4$; **Figure 5c**) and a positive correlation with HREE ($r = 0.3$) (**Supplementary Figure 3**).

MI show varying degrees of Sr enrichment and depletion from the expected concentration (Sr). Sr is determined using the relative compatibility of the neighboring REE in order of compatibility, Ce and Nd, using $Sr* = \left[{}^{[Ce]_{MI}}/_{[Ce]_{PM}} * {}^{[Nd]_{MI}}/_{[Ce]_{PM}} \right]^{1/2}$, where [Ce] and [Nd] are the concentration of these elements in either MI or primitive mantle (PM) [*Sobolev and Nikogosian*, 1994]. Sr/Sr* >1 suggests enrichment in Sr compared to the expected concentration based on compatibility, and Sr/Sr* suggests depletion in Sr. All FS melts have Sr/Sr* >1 and Sr enrichment is greatest for the relatively LREE-depleted 1669 melts. Sr depletion scales with LREE-enrichment and increasing LREE/HREE ratios (**Figure 5c**, **Supplementary Figure 4**). Enrichment in fluid mobile elements, such as Ba, appears to correlate with LREE-enrichment but not with Sr enrichment (**Supplementary Figure 3**).

4.4 Melt inclusion volatile systematics

H_2O concentrations in the 1669 melt inclusions exhibit a limited variability, with a range of 1.2-1.7 wt.% H_2O and a median of 1.4 wt.% (**Figure 6a**). Matrix glasses contain <0.6 wt.% H_2O. The limited range and low values reflect either their entrapment pressure or their diffusive equilibration during storage at low pressures (70-100 MPa) in the crust [*Bucholz et al.*, 2013; *Gaetani et al.*, 2012]. As the H_2O concentrations may be re-set to low pressure conditions by diffusive re-equilibration and be unrepresentative of their entrapment pressure.

CO_2 concentration in the melt inclusions varies from 40 to 1220 ppm; CO_2 concentrations in matrix glasses are below detection (20 ppm; gray triangles, **Figure 6a**). Sulfur concentrations in the melt inclusions vary between 80 and 1900 ppm (**Figure 6b**). Carbon and sulfur in melt inclusions correlate well with one another (r = 0.73, **Figure: 6b**, **Supplementary Figure 3**). Perhaps the most striking feature, however, of the covariance structure for the A.D. 1669 melt inclusion geochemistry is that CO_2 and sulfur both correlate negatively with incompatible elements such as Nb, LREE, Ba and Zr (**Figure 6c**). For the A.D. 1669 data alone, the correlation between CO_2 and Nb, for example, has an r value of -0.68 (CO_2 and e.g Ce, r = -0.59; Ba, r = -0.51; Zr, r = -0.59, **Supplementary Figure 3**). The most CO_2-rich and S-rich melts are those with lowest Ce/Y and Ce/Y has negative correlation with CO_2 and S with r values of -0.77 and -0.70 respectively. CO_2, however, correlates well with Sr and Sr/Sr (r = 0.63, 0.67 respectively, **Figure 6d**, **Supplementary Figure 3**). Fluorine shows a high degree of variability (0.14 - 0.24 wt.%) with no correlation with either host olivine Fo mol%

or degree of melt enrichment. Chlorine shows moderate variability (0.16 - 0.38 wt.%) with a weak negative correlation with LREE enrichment (r = -0.2) and weak positive correlations with HREE (r = 0.5) and host Fo content (r = -0.4).

5 Discussion

We have shown above that the 1669 melts, trapped in olivine, exhibit a linear mixing array of compositions, with one end member enriched in LREE (and Zr, Nb), depleted (relative to similarly compatible elements) in Sr and containing low concentrations of S and CO_2 (**Figures 5, 6; Supplementary Figures 3, 4**). The other end member melt is depleted in LREE, and relatively enriched in Sr, CO_2 and S. Fractionation of pyroxene is not capable of generating the range in, for example, Ce/Y observed in the melt inclusions (**Figure 5 a,b**); the range in Ce/Y (and in other LREE/HREE trace element ratios) must instead be inherited either from primary melts from the mantle or from modification of melts in the crust. Linear correlations between S and CO_2 in melt inclusions are not expected to result from degassing at Mt. Etna [*Spilliaert et al.*, 2006b], or elsewhere [*Métrich and Wallace*, 2008] owing to the much lower solubility of CO_2 in silicate melts over sulfur [*Witham et al.*, 2012]. These trends instead indicate an intrinsic relationship between trace element ratios and volatile systematics generated by processes beyond simple fractional crystallization and degassing. We propose that this array was generated by mixing the two liquids in a shallow magma reservoir prior to eruption, where the mixing process was 'captured' by the entrapment of melt inclusions. We discuss below why we believe that the LREE-depleted, Sr, C and S-rich end member may have ascended rapidly from depth, supersaturated. First, however, we consider how the relatively evolved 1669 end members of the mixing array may have been generated by fractional crystallization of primitive melts beneath Mt. Etna (exemplified by the primitive FS tephra melts [*Kamenetsky et al.*, 2007]), then we discuss the possible origin of the LREE-depleted, Sr, C and S-rich end member in terms of mantle and crustal processes.

5.1 Modelling fractional crystallization of two geochemically distinct melts

The primitive melt observed as melt inclusions from the FS eruption [*Kamenetsky et al.*, 2007] was used as a starting composition to model fractional crystallization (using Petrolog3; [*Danyushevsky and Plechov*, 2011a]) at NNO+1 [*Metrich and Clocchiatti*, 1996], 1100 °C [*Kamenetsky and Clocchiatti*, 1996] and for two pressures: 100 MPa [*Kahl et al.*, 2017] and 400 MPa [*Kamenetsky et al.*, 2007], which might be suitable for FS melt fractionation. We use examples of enriched and depleted (as indicated by Ce/Y) FS melt inclusions as a starting

point for the modeling because a) the FS melt inclusions are the most primitive to be observed at Mt. Etna, at ~13 wt% MgO (other primitive whole rocks have < 9 wt% MgO; [*Corsaro and Métrich*, 2016]) and b) the FS melt inclusions exhibit a similar range in Ce/Y to the 1669 melt inclusions, which is independent of fractional crystallization and c) a full set of compositional data (volatiles, major and trace elements) is available for the FS melt inclusions. We recognize, however, that previous studies have identified that the FS tephra has anomalously high CaO compared to other Mt. Etna magma compositions, as well as high radiogenic Sr and Rb/Th, which has been ascribed to a high degree of melting of a mantle source with considerable pyroxenite component [*Corsaro and Métrich*, 2016].

Fractional crystallization trends from Petrolog [*Danyushevsky and Plechov*, 2011a] at 100 and 400 MPa are marked onto **Figure 3** using the most depleted and enriched end member FS melts as a starting point for each pressure. The melts erupted during the A.D. 1669 and other recent eruptions have undergone fractionation of augite, as shown by the inflection point on the liquid line of descent (LLD) at 9 wt.% MgO where CaO begins to be depleted in the melt (**Figure 3**). Plagioclase crystallization begins at ~4 wt.% MgO, shown by depletion in both Al_2O_3 and CaO together (**Figure 3**). The fractional crystallisation models, where the order of crystallisation is: olivine→olivine+augite→olivine+augite+plagioclase, describes well the Al_2O_3 and CaO contents of the melts, although cannot reproduce the observed K_2O and Na_2O concentrations, which are higher than predicted from the models (**Figure 3 b,d**). This may be a consequence of the relatively low alkali content of the FS melts compared to other magma compositions from Mt. Etna, as identified previously [*Corsaro and Métrich*, 2016]. However, the models describe the evolution of the trace element concentrations well. We find that 70% fractional crystallization at 1 kbar of the least LREE-enriched FS melt (melts with the lowest Ce/Y; **Figure 5a**) [*Kamenetsky et al.*, 2007] yields a melt with the same LREE/HREE ratio as the least enriched melts in the A.D. 1669 melt inclusions (Ce/Y 2-3), with a similar absolute concentration of trace elements (**Figure 5a**). In the same way, 70% fractional crystallization of the most LREE-enriched FS melt (with Ce/Y 6) yields the observed LREE absolute concentrations of the enriched melts (with Ce/Y 6) of the A.D. 1669 inclusion suite.

We propose that the array of evolved compositions in the A.D. 1669 melt inclusions requires up to 70% fractionation of two primitive melt compositions that have similar end-member

trace element compositions to the FS melt but may be more alkali-rich. The LREE-depleted and LREE-enriched melts mix (to produce the observed melt inclusion array) only after each has undergone significant differentiation, thus yielding the observed high trace element compositions and the array in LREE/HREE observed in the 1669 MI suite (Ce/Y: 2-6, Nb 50-140, La 60-140) (**Figures 4, 5**). Mixing and fractionation was not concurrent because a) the trace element array seen in the 1669 melt inclusions is associated with a limited range in the MI major elements and is not systematic with the evolution of the olivine Fo mol.% and b) melt inclusions within a single olivine crystal can have the full range of enrichment and absolute trace element concentration observed in the entire dataset (**Supplementary Figure 2**). We have therefore established that the two end member melts that mixed to form the 1669 compositional array could feasibly have formed from the fractional crystallisation of liquids similar to the two extreme compositions sampled by the melt inclusions in the primitive FS tephra [*Kamenetsky et al.*, 2007]. But what then is the origin of the LREE, Sr and volatile systematics of the two end member melts? Did these melts acquire their geochemical features in the mantle or in the crust?

5.2 Sr-enrichment in 1669 depleted melts

Principal Component Analysis (PCA) of the 1669 melt inclusion trace element compositions indicates that the first two principal components describe 50% of the variance in trace element dataset (see **Supplementary Material**). The first principal component (PC1) highlights an anomaly in the behaviour of Sr, caused by a process that is fractionating Sr from other elements (**Supplementary Figure 5**). PC1 may be due to addition or removal of plagioclase (Sr is compatible in plagioclase while all other REE are incompatible and become enriched in the melt), or assimilation of Sr from some source or contaminant and this may also affect the different PC1 scores of HREE compared to LREE. PC2 is positive for the LREE and negative for the HREE (**Supplementary Figure 5**) and might therefore be related to (1) the depth of melting and the presence of garnet in the melting region where HREE are compatible, (2) the degree of mantle melting, which affects the degree of LREE enrichment, or (3) the trace element composition of the mantle source. The process controlling PC2 is responsible for the observed range in LREE/HREE of the end member melts. Sr, however, does not behave like the LREE as expected (**Figure 4c**, **Supplementary Figure 3**). Sr has a negative PC2 like the HREE, and this is likely to be due to the combined effect of the strontium anomaly with non-orthogonal mantle and crustal processes (**Supplementary Figure 5**). The PCA approach has not managed to clearly separate out the processes here.

The crucial difference between PC1 and PC2 is in the behaviour of the MREEs (**Supplementary Figure 5**) and this is important for understanding the controlling processes.

The abundance of Sr in both the primitive FS melts and the 1669 LREE-depleted melts is anomalous, as Sr is enriched with respect to its compatibility compared to other REE, i.e. Sr/Sr* (**Figure 5**; **Supplementary Figure 4**). There is a strong negative correlation between Sr/Sr* in the melt inclusions and LREE (La, Ce), Ba, Nb, Zr (r = -0.82 to -0.71); and a strong positive correlation between Sr/Sr* and CaO, CO_2 and S (r= 0.57 to 0.67) (**Supplementary Figure 3**). In the case of the FS melts, these correlations cannot be explained using olivine fractional crystallization alone (or the post-entrapment crystallisation of olivine on the melt inclusion walls) since this should affect elements with neighboring compatibility (Sr, Ce and Nd) in a similar way. A number of processes that affect Sr enrichment in the FS primitive melts and the more evolved 1669 melts are considered here.

Sr enrichment in melt inclusions may be caused by: (1) involvement of a Sr-rich mantle source component either from pyroxenite [*Correale et al.*, 2012] or a 'ghost plagioclase' signature inherited from an eclogitic component in the mantle source [*Sobolev et al.*, 2000]; (2) plagioclase assimilation within the crust by primitive melts [*Danyushevsky et al.*, 2003], in which LREE are highly incompatible; (3) accumulation of small fraction lower crustal gabbroic melts [*Annen et al.*, 2005]; (4) assimilation of crustal carbonate over a range of pressure and temperature [*Carter and Dasgupta*, 2015; *Marziano et al.*, 2008; *Michaud*, 1995]. The two potential sources of Sr, one from the mantle (eclogitic oceanic crust and/or a pyroxenite source) and one from the crust (plagioclase, gabbroic cumulates or carbonates), would have quite different implications for the volatiles, in particular the flux of volcanic carbon, as (a) the solubility of volatiles in silicate melts is dependent on the major element composition of the melt [*Moore*, 2008]; and (b) because some of these mechanisms involve volatile-rich sources (e.g. crustal carbonate and/or recycled lithologies). We discuss each of these mechanisms in turn.

5.2.1 Mantle source heterogeneity as the source of the Sr anomaly

Trace element and Sr isotope data for dyke-fed eruptions have revealed that mantle source heterogeneities, and particularly the variable involvement of a clinopyroxenitic lithology, have a strong influence over the degree of melting of the heterogeneous mantle and long-term magmatic processes beneath Mt. Etna [*Corsaro and Métrich*, 2016]. The Sr anomaly in the

primitive melts could, therefore, be inherited from the mantle due to incorporation of (i) small fractions of pyroxenite melt [*Correale et al.*, 2012; *Correale et al.*, 2014] or (ii) melts of recycled lower oceanic crustal plagioclase-bearing cumulates in the melting region. In the mantle melting region under Mt. Etna the restite of these recycled materials will be plagioclase free (e.g. eclogite), with a low bulk partition coefficient for Sr. Melts derived from recycled cumulates may therefore inherit the positive Sr/Sr anomaly of their sources [*Sobolev et al.*, 2000].

We explore the possible mantle origins of compositional variation in the melt inclusion suite by modelling incremental fractional melting of KLB-1 peridotite [*Davis et al.*, 2009; *Jennings and Holland*, 2015] and KG1(8) pyroxenite [*Jennings et al.*, 2016; *Kogiso et al.*, 1998] at 1315 and 1500 °C after [*Jennings and Holland*, 2015] and [*Jennings et al.*, 2016] respectively using pressure-temperature-melt fraction pathways for decompression melting calculated assuming anhydrous and isentropic conditions according to [*Katz et al.*, 2003] (further details are given in the **Supplementary Material**). Instantaneous 0.01 melt fractions were generated by the model and accumulated to obtain the trace element composition of melt fractions from 0 to 0.2. There are numerous solutions that can generate the FS melt end-member LREE/HREE ratios using a combination of the degree of melting of both sources and the degree of mixing between them (**Figure 7a**). A 10% pyroxenite, 90% peridotite composition has been proposed previously for FS melts using mantle xenoliths [*Correale et al.*, 2012], but our modeling suggests this solution is non-unique given the degrees of freedom in a combination of melt fraction and proportions of mixing sources. A more concrete result of the modeling is that there is no solution that gives a melt with both Sr enrichment and LREE-depletion (**Figure 7**).

An eclogite melting signature (associated with melting of recycled gabbroic cumulates) was proposed to explain the geochemistry of melt inclusions in olivines from Mauna Loa, Hawaii [*Sobolev et al.*, 2000]. Sr-rich melts from Mauna Loa show depletion in incompatible elements, including negative Nb and Zr anomalies [*Sobolev et al.*, 2000]. This distinctive trace element signature may be inherited from plagioclase, as is commonly observed in ophiolitic cumulates. It is proposed that gabbro may retain its chemical identity throughout convective cycling in the mantle without mixing with other parts of the subducted oceanic crustal sequence, yielding a 'ghost plagioclase' signature and Sr anomalies in the resulting ocean island melts. Melting models for different mantle sources show that eclogite melts are

very small in volume and are readily lost in the bulk magma but even a small fraction of eclogite-derived melts can have a significant effect on the REE chemistry. A mixture of 90% peridotite melt and 10% eclogite-derived melt provide a possible explanation for the observed REE and major element chemistry seen at Mauna Loa [*Sobolev et al.*, 2000]. The same geochemical anomalies as observed in the Mauna Loa melt inclusions [*Sobolev et al.*, 2000] are observed in the Sr-rich, LREE-depleted FS and 1669 melts (**figure 5**), making melting of recycled gabbroic cumulates in the mantle source region a plausible explanation for the presence of such anomalies.

5.2.2 Resorption of plagioclase as the source of the Sr anomaly

Early-formed plagioclase crystals trapped in MI can react with the host olivine and melt at high magmatic temperatures, resulting in a Sr-enriched melt composition [*Danyushevsky et al.*, 2003; *Schiavi et al.*, 2015] (**Figure 7b**). Plagioclase assimilation by complete dissolution was modeled using a plagioclase composition from a Mt. Etna eruption [*Viccaro et al.*, 2006] that was similar in composition to the 1669 eruption [*Corsaro et al.*, 1996]. The blue line in **Figure 7b** shows that up to 30% plagioclase dissolution is required to be mixed with the FS depleted end-member to give a melt composition that, after fractional crystallization, will have a high enough Sr concentration to match the LREE-depleted 1669 melts. However, complete dissolution is not realistic and plagioclase reacts incongruently in the melt inclusion according to plagioclase + melt + host olivine→ spinel + olivine + melt [*Danyushevsky et al.*, 2003]. Overall, the vector describing the progressive assimilation of plagioclase is inconsistent with the trends seen in the 1669 major and trace element data (vectors, **Figure 3, 7**).

5.2.3 Lower crustal gabbro assimilation as the source of the Sr anomaly

Localised re-melting of lower crustal gabbroic material is possible by fluid-rich, metasomatised mantle melts with a more primitive bulk composition to the lower crust [*Annen et al.*, 2005] (**Figure 7b**). Assimilation of gabbro was modeled for the Etnean AMLG gabbro (enclosed in 2001 lavas), with the highest whole rock Sr [*Corsaro et al.*, 2014] (pink box 1, **Figure 7b**). Melting of this gabbro (10%) was modeled using a batch melting equation (see **Supplementary Material,** Equation 1) and mixed with the enriched end-member of the FS melt to determine whether gabbroic assimilation could yield the positive Sr anomaly (and LREE depletion) described by the 1669 melts (pink line, pink box 2 indicates 10% melted

gabbro composition, **Figure 7b**). Addition of gabbroic melts, even with 100% mixing, did not give comparable Sr concentrations, primarily because the bulk solid-melt partition coefficient for Sr is too high. Nor did the REE become fractionated enough to reduce the LREE/HREE ratio and give a more depleted melt signature, comparable to the 1669 depleted MI. Additionally, progressive assimilation of gabbro does not follow the major element oxide trends seen in 1669 MI (**Figure 3**). We therefore reject re-melting of gabbro as a mechanism to generate the observed Sr anomaly and LREE depletion observed in the FS and 1669 melt inclusions.

5.2.4 Magmatic assimilation of crustal carbonate and/or associated fluids

A potential source of Sr is carbonate melt or fluid assimilation during transport and storage of melts in the 40 km thick Etnean crust. The whole rock Sr isotope composition of the 1669 lavas ranges from 0.70330 to 0.70344 and are very similar to MORB [*Corsaro et al.*, 1996]). This low radiogenic Sr isotopic composition does not preclude assimilation of Sr from Cretaceous carbonates, however, which have Sr/Sr isotope of 0.707 and are significantly less radiogenic than the continental crust (mean 0.716) [*Elderfield*, 1986].

Carbonate assimilation is modeled using a carbonate xenolith found in 1982 lava [*Corsaro et al.*, 2014]. Addition of carbonate to the FS LREE-enriched end-member (green line, **Figure 7b**) yields a higher Sr concentration in the melt but reduces the LREE concentration, giving a more depleted LREE/HREE, but Sr-enriched melt. Melt compositions generated by 40-50% assimilation of carbonate into the enriched melt and up to 70% fractional crystallization are very similar to the LREE-depleted and Sr-rich end-member melt of the 1669 eruption (**Figure 7**). The carbonate assimilation here is the maximum possible since it is assumed here that an enriched-FS end member melt is the parental melt, when in fact the depleted 1669 melt inclusions may have been sourced from a more depleted primitive melt. It is possible that both parental melts have undergone some carbonate assimilation before mixing and by different amounts, with the more depleted parental melt assimilating more carbonate so as to result in a greater Sr anomaly than the enriched melt.

However, assimilation of these high percentages of carbonate material is unrealistic when we consider their potential effect on major element oxides (**Figure 3**). Assimilation of carbonate causes an increase in the CaO content of the melt (vectors: **Figure 3c**) and increased clinopyroxene (cpx) nucleation and crystallization with compositional progression towards

Ca-Tschermak cpx [*Mollo et al.*, 2010]. This depletes the melt in MgO and SiO_2, consumes olivine and plagioclase and crystallizes scapolite and spinel, thus changing the modal proportions of phases in the system [*Carter and Dasgupta*, 2015; *Marziano et al.*, 2008; *Mollo et al.*, 2010]. The model results in an enrichment of alkalis in the melt (**Figure 3b,d**) as these are not compatible in cpx. The degree of assimilation, the resulting phase assemblage and melt composition, and the CO_2 fluid release is PT dependent, with LP and HT conditions having the greatest assimilation potential. Experiments show that at 0.5 GPa 21-48% carbonate can be assimilated between 1100 °C and 1200 °C and the CO_2 fluid produced at 1 GPa between 1100 °C and 1175 °C increases from 0.09 to 0.28 g per gram of basaltic melt [*Carter and Dasgupta*, 2015]. The CO_2-rich fluid phase causes dehydration of the melt and increases the CO_2/H_2O ratio of the free fluid phase. The enhanced CO_2 fugacity in the fluid phase and the increased melt CaO content may increase the solubility of CO_2 in the melt. The composition of the C-O-H fluid affects the redox state of the carbonated system and experiments by [*Mollo et al.*, 2010] show fO is lowered by two log units when a CO_2-rich C-O-H fluid is present. However, fluid migration away from the reservoir may cause the opposite effect.

The extent of carbonate assimilation is limited by the MgO content of the system [*Carter and Dasgupta*, 2015]. Melts at Vesuvius are phonolitic in composition due to a reduction in MgO and enrichment in alkalis, and show evidence for carbonate assimilation [*Carter and Dasgupta*, 2015; *Freda et al.*, 2008]. Progressively more carbonate assimilation leads to alkali-rich, MgO-poor and SiO_2-poor melts that are foiditic in composition, such as those from the Colli Albani Volcanic District [*Freda et al.*, 2008; *Gaeta et al.*, 2009]. Oxygen isotopes support carbonate assimilation by these magmas, as well as the presence of skarns and the high CO_2 flux from Italian volcanic systems [*Chiodini et al.*, 2004]. For Mt. Etna it has been estimated that 41-92% of magma (the experiments used a synthetic K-basalt) would need to react with calcite to explain the observed emission rate of CO_2 [*Carter and Dasgupta*, 2015]. The 1669 melts, however, are not ultra-calcic and silica-poor as would be expected from the percentage of carbonate required to yield the Sr anomaly (**Figure 7**). However, the depleted 1669 melts do show a higher CaO content (**Figure 3c**) than the enriched melts.

5.3 The implications of melt heterogeneity for volatile systematics

The negative correlation between CO_2 and Nb (r = -0.68, **Figure 6c**, **Supplementary Figure 3**) contrasts with the positive correlation measured in vapor-undersaturated melt inclusions

600 from the Siqueiros fracture zone on the East Pacific Rise [*Saal et al.*, 2002] and calculated for
601 undegassed Mid-Atlantic Ridge basalts [*Cartigny et al.*, 2008]. Other CO_2-trace element
602 datasets in the literature either record significant variability in CO_2 with near-constant Nb
603 [*Shaw et al.*, 2010], or show no robust correlations between the two species [*Dixon and*
604 *Clague*, 2001; *Helo et al.*, 2011; *Koleszar et al.*, 2009; *Workman et al.*, 2006]. Melt
605 inclusions are usually partly degassed with respect to CO_2 and this lack of correlation
606 commonly reflects this. A negative correlation between CO_2 and incompatible trace elements
607 was observed in a melt inclusion suite from Skuggafjöll, Iceland [*Neave et al.*, 2014] and
608 could arise during olivine cooling, post-entrapment crystallization and the formation of a
609 shrinkage bubble . However, the low degree of PEC (5-10%; **Supplementary Table 5**)
610 observed in the 1669 melt inclusions and analysis of shrinkage-bubble-free MI means that the
611 full range in incompatible element concentrations is not reproducible with this mechanism.
612 Modeling of mid-ocean ridge volatile systematics has shown this negative correlation may
613 also arise during concurrent mixing and degassing at a range of pressures [*Matthews et al.*,
614 2017], although this mechanism cannot reproduce the CO_2-Sr-REE systematics we observe
615 for the 1669 melt inclusions.
616
617 We propose that the positive correlation between Sr and CO_2 ($r = 0.63$) and between Sr/*Sr (r
618 $= 0.67$) observed in the melt inclusion suite represents a mixing signature, as discussed
619 above. In order for two equilibrium melts, with different CO_2 concentrations, to mix at the
620 same pressure requires the solubility of CO_2 in the two melts to be different [*Dixon*, 1997;
621 *Shishkina et al.*, 2014]. The depleted and enriched melts observed in both the 1669 and FS
622 melt inclusion suites (one with low LREE and high Sr, the other with high LREE and low Sr)
623 have different major element oxide compositions, with up to 2 wt.% differences in CaO, KO,
624 NaO and AlO (**Figure 3**). These differences are sufficient to cause differences in CO_2
625 solubility. Melts that are rich in calcium (Ca) and alkalis (K and Na) stabilise higher
626 concentrations of CO_2 [*Moore*, 2008; *Shishkina et al.*, 2014]. Sulfur fluid-melt partitioning is
627 also reduced as the mole fraction of Ca and Al in the melt increases [*Zajacz*, 2015] leading to
628 the melt being able to dissolve more sulfur (in the absence of sulfide or sulfate saturation).
629 Differences in major element composition between the two end member melts may explain
630 the strong correlation between CO_2 and S ($r = 0.73$), and the negative correlations between
631 CO_2 and LREE ($r = -0.68$ to -0.59) and positive correlations between CO_2 and Sr ($r = 0.63$),
632 which are not consistent with degassing trends. A degassing trend would deplete CO_2 at

633 greater pressures than S, resulting in an array of shallow-trapped melts with low CO_2 and
634 variable sulfur. For a degassing trend alone, correlations between CO_2 and S and LREE and
635 Sr would not be expected. For CO_2 fluxing and degassing-induced crystallisation [*Cashman*
636 *and Blundy*, 2000], trends of increasing CO_2, decreasing S and increasing LREE would be
637 expected, which are not observed (**Figure 6**).
638
639 The major element parametrization of CO_2 solubility [*Shishkina et al.*, 2014] (**Figure 8**)
640 yields equilibrium pressures of ~200 MPa for the high-CO_2 FS melt inclusions (rather than
641 400 MPa using VolatileCalc; [*Kamenetsky et al.*, 2007; *Newman and Lowenstern*, 2002])
642 because these melts are rich in Ca and alkali elements, which enhances the solubility of CO_2.
643 The different solubilities for the depleted and enriched FS melts (red circles, low and high
644 Ce/Y; **Figure 8a**), caused by their different CaO and alkali contents, provides a mechanism
645 for CO_2-rich and CO_2-poor melts to mix at the same pressure, at ~200 MPa (**Figure 8b**),
646 rather than over the range 380-500 MPa as predicted by a solubility model that does not
647 include compositional dependence [*Kamenetsky et al.*, 2007]. It is important to note,
648 however, that the FS melt inclusions contain shrinkage bubbles which may have sequestered
649 some CO_2 (there are three FS melt inclusions with CO_2 < 1000 ppm) [*Kamenetsky et al.*,
650 2007]; hence the actual trapping pressure was likely higher. For the 1669 melt inclusions
651 (orange triangles; **Figure 8**), those with the highest CO_2 (>500 ppm) are the most depleted in
652 their LREE contents (Ce/Y < 4), and are also richer in Ca and Mg but poorer in alkalis
653 (**Figure 3**) which yields a mean equilibration pressure of ~150 MPa (**Figure 8b**), although
654 there is considerable scatter [*Shishkina et al.*, 2014]. However, the differences in major
655 element composition and CO_2 solubility for the 1669 melt inclusions cannot entirely
656 reconcile their saturation pressures (**Figure 8b**), with the more enriched melts (Ce/Y > 4)
657 exhibiting a large range (20-180 MPa) and a lower mean (70 MPa) equilibration pressure
658 than the depleted melts (with Ce/Y < 4; **Figure 8b**). If the melt inclusions were all entrapped
659 together, in one shallow storage region, one might expect them all to record similar
660 equilibration pressures, yet this is clearly not the case.
661
662 Another possibility to explain the observed range in 'apparent' pressures for the mixing array
663 (orange triangles, **Figure 8b**) is that the depleted end-member melt may be supersaturated
664 with respect to carbon and sulfur upon mixing. Supersaturation may develop when basalts
665 ascend from magma reservoirs to the surface faster than CO_2 can diffuse into bubbles, e.g. as
666 proposed for the Skuggafjöll melt in the Eastern Volcanic Zone of Iceland [*Neave et al.*,

2014], or in submarine basaltic glasses where CO_2 concentrations often exceed the equilibrium concentrations predicted from solubility models [*Dixon et al.*, 1988; *Helo et al.*, 2011; *Soule et al.*, 2012]. Experiments were carried out to investigate the vesiculation of basalts from Stromboli [*Pichavant et al.*, 2013]. Natural pumice and glass samples were used to simulate melt ascent from 2-2.5 kbar to 0.25-0.5 kbar and it was found that, at a decompression rate equivalent to an ascent rate of 0.25 to 1.5 m/s, CO_2 concentrations were up to an order of magnitude higher than the solubility at the final pressure, corresponding to supersaturation pressures of ~ 150 MPa. At low vesicularity and/or bubble number density, CO_2 exsolution was limited by the rate of CO_2 diffusion through the melt, rather than the rate of CO_2 transfer across melt/vesicle interfaces, resulting in disequilibrium degassing (similar to rhyolite studies; [*Mangan and Sisson*, 2000]). The composition used by [*Pichavant et al.*, 2013] is slightly more hydrous (2.7 - 3.8 wt.%) than the 1669 Mt. Etna samples (1.4 wt.%), but the CO_2 content is very similar (up to 1200 ppm). The ascent timescales for the melt to become CO_2 supersaturated upon arrival into a shallow magma reservoir is on the order of hours to days, depending on the vesicle number [*Neave et al.*, 2014], which is comparable to the ascent times from reservoir depths estimated for Etnean eruptions of a few hours (from seismicity during the explosive flank eruption in 2002 at Mt. Etna, [*Patanè et al.*, 2003]), or a few days (from the A.D. 1669 contemporary records of vigorous seismic events preceding the A.D 1669 eruption by 2 weeks and focused at the eventual site of the Monti Rossi cone [*Mulas et al.*, 2016; *Tanguy et al.*, 1996] and references therein). Sulfur is strongly positively correlated with CO_2 ($r = 0.73$) (**Supplementary Figure 3**), suggesting that the depleted melt may also be supersaturated in sulfur upon mixing, consistent with the similar diffusivities of CO_2 and S in basaltic melts [*Baker et al.*, 2005; *Freda et al.*, 2005].

6 Implications and comparison with previous work

Melt inclusions hosted by olivines erupted during the initial stages of the 1669 eruption of Mt. Etna, Italy, preserve a record of melt mixing. Two relatively evolved basaltic melts (each had undergone ~ 70% fractional crystallization) mixed to form an array of compositions with one end member (perhaps slightly more primitive) depleted in LREE, enriched in Sr, Ca, carbon and sulfur intruding a shallow storage region containing a melt relatively enriched in LREE, and relatively depleted in Sr, carbon and sulfur. We propose that the LREE-depleted melt, which was rich in Sr, may have been generated by either the incorporation of a melt derived from a Sr-enriched recycled cumulate gabbro in the mantle, or by incorporation of crustal carbonate. In either case, the modification in major element (Ca, Na and K, in

701 particular) composition of the melt caused the solubility of carbon and sulfur in the melt to
702 increase. Rapid rise of such depleted, volatile-rich melts may have cause the melt to become
703 supersaturated, such that upon arrival into the shallow plumbing system, where the melts
704 stalled and mixed with resident melts, a vigorous episode of degassing would have taken
705 place, both in response to rapid equilibration, but also in response to cooling upon mingling
706 with the stored melts. This cooling would have caused a burst of crystal growth, allowing
707 melt inclusions to be trapped which recorded the mingling and mixing of these two distinct
708 melts.
709
710 Magma mixing prior to and during the 1669 eruption of Mt. Etna is consistent with previous
711 work. Corsaro et al. [*1996*] identified two lava types based on their geochemistry: SET1 and
712 SET2. SET1 was erupted during 11-20 March 1669 and were more promitive than the later-
713 erupted SET2. The lava types were interpreted as having coexisted and interacted in the
714 magmatic storage system prior to eruption, with the lower density, volatile-rich SET1 magma
715 rising up through the SET2 magma. Kahl et al. [*2017*] deduced additional detail from study
716 of olivine core and rim compositions, combined with timescales from diffusion modeling.
717 SET1 magmas contained olivines with core compositions similar (Fo_{75-78}) to those we
718 analyse in this study (Fo_{74-75}) [*Kahl et al., 2017*]. The magma was invaded by a more evolved
719 melt 1-2 years prior to eruption, which gave rise to the lower forsterite rims, which continued
720 up to a few weeks or months prior to eruption [*Kahl et al., 2017*]. The intruding melts
721 ascending rapidly up to shallow levels in the system may have carried high fractions of
722 exsolved (and dissolved) volatiles.
723
724 Mixing between supersaturated melts (with their bulk CO_2 content enhanced by due to their
725 Ca- and alkali-rich composition) and stored, degassed melts shortly before eruption may
726 explain observations of enhanced CO_2 fluxes prior to eruptions at Mt. Etna [*Aiuppa et al.*,
727 2007; *Aiuppa et al.*, 2008]. Mixing of magmas with markedly different compositions (mafic
728 injected into more evolved magmas) has been proposed as a means to trigger eruptions at
729 many stratovolcanoes [*Venezky and Rutherford*, 1997; *Woods and Cardoso*, 1997] but in the
730 case of 1669 and recent eruptions at Mt. Etna [*Ferlito et al.*, 2010; *Métrich et al.*, 2004;
731 *Viccaro et al.*, 2006] both mixing magmas have a basaltic composition. The critical factors
732 controlling eruption triggering may be the differential volatile contents and solubility in the
733 melt due to differences in major element composition. Evidence is presented that indicates
734 that incompatible element-depleted melts may ascend rapidly through the mid- and upper

crust beneath Mt. Etna, developing supersaturation in the volatiles carbon dioxide and sulfur and thereby suppressing their outgassing into a vapor phase. The arrival of these melts into shallow magma storage areas may prompt rapid cooling and vesiculation, the conditions necessary to trap melt inclusions (during rapid crystal growth) and to trigger eruptions (through vesiculation and increase in overpressures). This process of intrusion of volatile-charged, supersaturated melts may be a common process not only at Mt. Etna, but also at many other basaltic volcanoes worldwide. This study further supports the growing assertion that melt inclusion arrays of H_2O and CO_2 compositions only very rarely show degassing pathways; more commonly the diffuse array of data reflects composition-dependent solubility, disequilibrium (supersaturation in CO_2 over H_2O) and mixing.

Acknowledgements

This work was supported by a Natural Environment Research Council studentship to L. C. Salem (NE/L501578/1) and a Natural Environment Research Council Ion Microprobe Facility award (IMF483/0513). We thank Robin Clarke, Martin Walker and Iris Buisman for help with sample preparation and EPMA at the University of Cambridge. We thank all the staff, and Richard Hinton in particular, for their assistance with SIMS analyses at the Ion Microprobe Facility at University of Edinburgh. We thank David Neave for helpful discussions. We acknowledge insightful reviews from Nicole Métrich, Kayla Iacovino, Terry Plank, Eniko Bali and one anonymous reviewer which improved this manuscript enormously. We thank Associate Editor Tobias Fischer and Editor Claudio Faccenna for their handling of this manuscript. All the data used are listed in the references or contained within the Supplementary Material.

References

Aiuppa, A., C. Federico, G. Giudice, S. Gurrieri, M. Liuzzo, H. Shinohara, R. Favara, and M. Valenza (2006), Rates of carbon dioxide plume degassing from Mount Etna volcano, *Journal of Geophysical Research: Solid Earth (1978–2012)*, *111*(B9).

Aiuppa, A., R. Moretti, C. Federico, G. Giudice, S. Gurrieri, M. Liuzzo, P. Papale, H. Shinohara, and M. Valenza (2007), Forecasting Etna eruptions by real-time observation of volcanic gas composition, *Geology*, *35*(12), 1115-1118.

Aiuppa, A., G. Giudice, S. Gurrieri, M. Liuzzo, M. Burton, T. Caltabiano, A. McGonigle, G. Salerno, H. Shinohara, and M. Valenza (2008), Total volatile flux from Mount Etna, *Geophysical Research Letters*, *35*(24).

Allard, P., B. Behncke, S. D'Amico, M. Neri, and S. Gambino (2006), Mount Etna 1993–2005: anatomy of an evolving eruptive cycle, *Earth-Science Reviews*, *78*(1), 85-114.

772 Allard, P., J. Carbonnelle, D. Dajlevic, J. Le Bronec, P. Morel, M. Robe, J. Maurenas, R.
773 Faivre-Pierret, D. Martin, and J. Sabroux (1991), Eruptive and diffuse emissions of CO2
774 from Mount Etna, *Nature*, *351*(6325), 387-391.
775 Aloisi, M., O. Cocina, G. Neri, B. Orecchio, and E. Privitera (2002), Seismic tomography of
776 the crust underneath the Etna volcano, Sicily, *Physics of the Earth and Planetary Interiors*,
777 *134*(3-4), 139-155.
778 Andronico, D., and R. Corsaro (2011), Lava fountains during the episodic eruption of South–
779 East Crater (Mt. Etna), 2000: insights into magma-gas dynamics within the shallow volcano
780 plumbing system, *Bull Volcanol*, *73*(9), 1165-1178.
781 Andronico, D., S. Branca, S. Calvari, M. Burton, T. Caltabiano, R. A. Corsaro, P. Del Carlo,
782 G. Garfì, L. Lodato, and L. Miraglia (2005), A multi-disciplinary study of the 2002–03 Etna
783 eruption: insights into a complex plumbing system, *Bull Volcanol*, *67*(4), 314-330.
784 Annen, C., J. Blundy, and R. Sparks (2005), The genesis of intermediate and silicic magmas
785 in deep crustal hot zones, *Journal of Petrology*, *47*(3), 505-539.
786 Baker, D. R., C. Freda, R. A. Brooker, and P. Scarlato (2005), Volatile diffusion in silicate
787 melts and its effects on melt inclusions, *Annals of Geophysics*, *48*(4-5).
788 Bottari, A., F. Broccio, and E. o GIUDICE (1975), Some seismologieal results and
789 geostructural suggestions from a study of the Reggio Calabria earthquake of 16 January,
790 1975, *Annals of Geophysics*, *28*(2-3), 219-239.
791 Branca, S., and V. Ferrara (2013), The morphostructural setting of Mount Etna sedimentary
792 basement (Italy): Implications for the geometry and volume of the volcano and its flank
793 instability, *Tectonophysics*, *586*, 46-64.
794 Branca, S., and L. Vigliotti (2015), Finding of an historical document describing an eruption
795 in the NW flank of Etna in July 1643 AD: timing, location and volcanic products, *Bull*
796 *Volcanol*, *77*(11), 95.
797 Branca, S., E. De Beni, and C. Proietti (2013), The large and destructive 1669 AD eruption at
798 Etna volcano: reconstruction of the lava flow field evolution and effusion rate trend, *Bull*
799 *Volcanol*, *75*(2), 694.
800 Bucholz, C. E., G. A. Gaetani, M. D. Behn, and N. Shimizu (2013), Post-entrapment
801 modification of volatiles and oxygen fugacity in olivine-hosted melt inclusions, *Earth and*
802 *Planetary Science Letters*.
803 Burton, M. R., G. M. Sawyer, and D. Granieri (2013), Deep carbon emissions from
804 volcanoes, *Rev. Mineral. Geochem*, *75*(1), 323-354.
805 Carter, L. B., and R. Dasgupta (2015), Hydrous basalt–limestone interaction at crustal
806 conditions: Implications for generation of ultracalcic melts and outflux of CO 2 at volcanic
807 arcs, *Earth and Planetary Science Letters*, *427*, 202-214.
808 Cartigny, P., F. Pineau, C. Aubaud, and M. Javoy (2008), Towards a consistent mantle
809 carbon flux estimate: Insights from volatile systematics (H< sub> 2</sub> O/Ce,< i> δD</i>,
810 CO< sub> 2</sub>/Nb) in the North Atlantic mantle (14° N and 34° N), *Earth and Planetary*
811 *Science Letters*, *265*(3), 672-685.
812 Cashman, K., and J. Blundy (2000), Degassing and crystallization of ascending andesite and
813 dacite, *Philosophical Transactions of the Royal Society of London. Series A: Mathematical,*
814 *Physical and Engineering Sciences*, *358*(1770), 1487-1513.
815 Catalano, S., S. Torrisi, and C. Ferlito (2004), The relationship between Late Quaternary
816 deformation and volcanism of Mt. Etna (eastern Sicily): new evidence from the sedimentary
817 substratum in the Catania region, *Journal of Volcanology and Geothermal Research*, *132*(4),
818 311-334.
819 Chiodini, G., C. Cardellini, A. Amato, E. Boschi, S. Caliro, F. Frondini, and G. Ventura
820 (2004), Carbon dioxide Earth degassing and seismogenesis in central and southern Italy,
821 *Geophysical Research Letters*, *31*(7).

Chiodini, G., D. Granieri, R. Avino, S. Caliro, A. Costa, C. Minopoli, and G. Vilardo (2010), Non - volcanic CO2 Earth degassing: Case of Mefite d'Ansanto (southern Apennines), Italy, *Geophysical Research Letters*, *37*(11).
Chiodini, G., S. Caliro, A. Aiuppa, R. Avino, D. Granieri, R. Moretti, and F. Parello (2011), First 13 C/12 C isotopic characterisation of volcanic plume CO 2, *Bull Volcanol*, *73*(5), 531-542.
Clocchiatti, R., and N. Metrich (1984), Témoignages de la contamination dans les produits des éruptions explosives des M. Silvestri (1892) et M. Rossi (1669)(M. Etna), *Bulletin Volcanologique*, *47*(4), 909-928.
Clocchiatti, R., J.-L. Joron, and M. Treuil (1988), The role of selective alkali contamination in the evolution of recent historic lavas of Mt. Etna, *Journal of Volcanology and Geothermal Research*, *34*(3-4), 241-249.
Collins, S. J., D. M. Pyle, and J. Maclennan (2009), Melt inclusions track pre-eruption storage and dehydration of magmas at Etna, *Geology*, *37*(6), 571-574.
Condomines, M., J.-C. Tanguy, and V. r. Michaud (1995), Magma dynamics at Mt Etna: constraints from U-Th-Ra-Pb radioactive disequilibria and Sr isotopes in historical lavas, *Earth and Planetary Science Letters*, *132*(1-4), 25-41.
Correale, A., M. Martelli, A. Paonita, A. Rizzo, L. Brusca, and V. Scribano (2012), New evidence of mantle heterogeneity beneath the Hyblean Plateau (southeast Sicily, Italy) as inferred from noble gases and geochemistry of ultramafic xenoliths, *Lithos*, *132*, 70-81.
Correale, A., A. Paonita, M. Martelli, A. Rizzo, S. G. Rotolo, R. A. Corsaro, and V. Di Renzo (2014), A two-component mantle source feeding Mt. Etna magmatism: Insights from the geochemistry of primitive magmas, *Lithos*, *184*, 243-258.
Corsaro, R., N. Métrich, P. Allard, D. Andronico, L. Miraglia, and C. Fourmentraux (2009), The 1974 flank eruption of Mount Etna: An archetype for deep dike - fed eruptions at basaltic volcanoes and a milestone in Etna's recent history, *Journal of Geophysical Research: Solid Earth*, *114*(B7).
Corsaro, R. A., and M. Pompilio (2004), Buoyancy - controlled eruption of magmas at Mt Etna, *Terra Nova*, *16*(1), 16-22.
Corsaro, R. A., and N. Métrich (2016), Chemical heterogeneity of Mt. Etna magmas in the last 15 ka. Inferences on their mantle sources, *Lithos*, *252*, 123-134.
Corsaro, R. A., R. Cristofolini, and L. Patanè (1996), The 1669 eruption at Mount Etna: chronology, petrology and geochemistry, with inferences on the magma sources and ascent mechanisms, *Bull Volcanol*, *58*(5), 348-358.
Corsaro, R. A., L. Miraglia, and M. Pompilio (2007), Petrologic evidence of a complex plumbing system feeding the July–August 2001 eruption of Mt. Etna, Sicily, Italy, *Bull Volcanol*, *69*(4), 401.
Corsaro, R. A., S. G. Rotolo, O. Cocina, and G. Tumbarello (2014), Cognate xenoliths in Mt. Etna lavas: witnesses of the high-velocity body beneath the volcano, *Bull Volcanol*, *76*(1), 772.
Cristofolini, R., and R. Romano (1982), Petrologic features of the Etnean volcanic rocks, *Mem. Soc. Geol. It*, *23*, 99-115.
Danyushevsky, L. V., and P. Plechov (2011a), Petrolog3: Integrated software for modeling crystallization processes, *Geochemistry, Geophysics, Geosystems*, *12*(7).
Danyushevsky, L. V., and P. Plechov (2011b), Petrolog3: Integrated software for modeling crystallization processes, *Geochemistry, Geophysics, Geosystems*, *12*(7), Q07021.
Danyushevsky, L. V., M. R. Perfit, S. M. Eggins, and T. J. Falloon (2003), Crustal origin for coupled'ultra-depleted'and'plagioclase'signatures in MORB olivine-hosted melt inclusions: evidence from the Siqueiros Transform Fault, East Pacific Rise, *Contr. Mineral. and Petrol.*, *144*(5), 619-637.

872 Davis, F. A., J. A. Tangeman, T. J. Tenner, and M. M. Hirschmann (2009), The composition
873 of KLB-1 peridotite, *American Mineralogist*, *94*(1), 176-180.
874 Dixon, J. E. (1997), Degassing of alkalic basalts, *American Mineralogist*, *82*, 368-378.
875 Dixon, J. E., and D. A. Clague (2001), Volatiles in Basaltic Glasses from Loihi Seamount,
876 Hawaii: Evidence for a Relatively Dry Plume Component, *Journal of Petrology*, *42*(3), 627-
877 654.
878 Dixon, J. E., E. Stolper, and J. R. Delaney (1988), Infrared spectroscopic measurements of
879 CO2 and H2O in Juan de Fuca Ridge basaltic glasses, *Earth and Planetary Science Letters*,
880 *90*(1), 87-104.
881 Doglioni, C., F. Innocenti, and G. Mariotti (2001), Why Mt Etna?, *Terra Nova*, *13*(1), 25-31.
882 Elderfield, H. (1986), Strontium isotope stratigraphy, *Palaeogeography, palaeoclimatology,*
883 *palaeoecology*, *57*(1), 71-90.
884 Ferlito, C., M. Viccaro, and R. Cristofolini (2008), Volatile-induced magma differentiation in
885 the plumbing system of Mt. Etna volcano (Italy): evidence from glass in tephra of the 2001
886 eruption, *Bull Volcanol*, *70*(4), 455-473.
887 Ferlito, C., M. Viccaro, E. Nicotra, and R. Cristofolini (2010), Relationship between the flank
888 sliding of the South East Crater (Mt. Etna, Italy) and the paroxysmal event of November 16,
889 2006, *Bull Volcanol*, *72*(10), 1179-1190.
890 Freda, C., D. R. Baker, and P. Scarlato (2005), Sulfur diffusion in basaltic melts, *Geochimica*
891 *et cosmochimica acta*, *69*(21), 5061-5069.
892 Freda, C., M. Gaeta, V. Misiti, S. Mollo, D. Dolfi, and P. Scarlato (2008), Magma–carbonate
893 interaction: an experimental study on ultrapotassic rocks from Alban Hills (Central Italy),
894 *Lithos*, *101*(3-4), 397-415.
895 Frezzotti, M. L., A. Peccerillo, and G. Panza (2009), Carbonate metasomatism and CO2
896 lithosphere–asthenosphere degassing beneath the Western Mediterranean: an integrated
897 model arising from petrological and geophysical data, *Chemical Geology*, *262*(1-2), 108-120.
898 Gaeta, M., T. Di Rocco, and C. Freda (2009), Carbonate assimilation in open magmatic
899 systems: the role of melt-bearing skarns and cumulate-forming processes, *Journal of*
900 *Petrology*, *50*(2), 361-385.
901 Gaetani, G. A., J. A. O'Leary, N. Shimizu, C. E. Bucholz, and M. Newville (2012), Rapid
902 reequilibration of H2O and oxygen fugacity in olivine-hosted melt inclusions, *Geology*,
903 *40*(10), 915-918.
904 Gerlach, T. M. (1991), Present‐day CO2 emissions from volcanos, *Eos, Transactions*
905 *American Geophysical Union*, *72*(23), 249-255.
906 Gvirtzman, Z., and A. Nur (1999), The formation of Mount Etna as the consequence of slab
907 rollback, *Nature*, *401*(6755), 782.
908 Halmer, M., H.-U. Schmincke, and H.-F. Graf (2002), The annual volcanic gas input into the
909 atmosphere, in particular into the stratosphere: a global data set for the past 100 years,
910 *Journal of Volcanology and Geothermal Research*, *115*(3), 511-528.
911 Hartley, M. E., J. Maclennan, M. Edmonds, and T. Thordarson (2014), Reconstructing the
912 deep CO< sub> 2</sub> degassing behaviour of large basaltic fissure eruptions, *Earth and*
913 *Planetary Science Letters*, *393*, 120-131.
914 Heap, M., S. Mollo, S. Vinciguerra, Y. Lavallée, K.-U. Hess, D. B. Dingwell, P. Baud, and
915 G. Iezzi (2013), Thermal weakening of the carbonate basement under Mt. Etna volcano
916 (Italy): implications for volcano instability, *Journal of volcanology and geothermal research*,
917 *250*, 42-60.
918 Helo, C., M.-A. Longpré, N. Shimizu, D. A. Clague, and J. Stix (2011), Explosive eruptions
919 at mid-ocean ridges driven by CO2-rich magmas, *Nature Geoscience*, *4*(4), 260-263.
920 Hirn, A., A. Nercessian, M. Sapin, F. Ferrucci, and G. Wittlinger (1991), Seismic
921 heterogeneity of Mt Etna: structure and activity, *Geophysical Journal International*, *105*(1),

139-153.
Jennings, E. S., and T. J. Holland (2015), A simple thermodynamic model for melting of peridotite in the system NCFMASOCr, *Journal of Petrology*, *56*(5), 869-892.
Jennings, E. S., T. J. Holland, O. Shorttle, J. Maclennan, and S. A. Gibson (2016), The composition of melts from a heterogeneous mantle and the origin of ferropicrite: application of a thermodynamic model, *Journal of Petrology*, *57*(11-12), 2289-2310.
Jochum, K. P., U. Nohl, K. Herwig, E. Lammel, B. Stoll, and A. W. Hofmann (2005), GeoReM: a new geochemical database for reference materials and isotopic standards, *Geostandards and Geoanalytical Research*, *29*(3), 333-338.
Jochum, K. P., U. Weis, B. Stoll, D. Kuzmin, Q. Yang, I. Raczek, D. E. Jacob, A. Stracke, K. Birbaum, and D. A. Frick (2011), Determination of reference values for NIST SRM 610–617 glasses following ISO guidelines, *Geostandards and Geoanalytical Research*, *35*(4), 397-429.
Kahl, M., M. Viccaro, T. Ubide, D. J. Morgan, and D. B. Dingwell (2017), A branched magma feeder system during the 1669 eruption of Mt Etna: evidence from a time-integrated study of zoned olivine phenocryst populations, *Journal of Petrology*, *58*(3), 443-472.
Kamenetsky, V., and R. Clocchiatti (1996), Primitive magmatism of Mt. Etna: insights from mineralogy and melt inclusions, *Earth and Planetary Science Letters*, *142*(3-4), 553-572.
Kamenetsky, V. S., M. Pompilio, N. Métrich, A. V. Sobolev, D. V. Kuzmin, and R. Thomas (2007), Arrival of extremely volatile-rich high-Mg magmas changes explosivity of Mount Etna, *Geology*, *35*(3), 255-258.
Katz, R. F., M. Spiegelman, and C. H. Langmuir (2003), A new parameterization of hydrous mantle melting, *Geochemistry, Geophysics, Geosystems*, *4*(9).
Kogiso, T., K. Hirose, and E. Takahashi (1998), Melting experiments on homogeneous mixtures of peridotite and basalt: application to the genesis of ocean island basalts, *Earth and Planetary Science Letters*, *162*(1-4), 45-61.
Koleszar, A. M., A. E. Saal, E. H. Hauri, A. N. Nagle, Y. Liang, and M. D. Kurz (2009), The volatile contents of the Galapagos plume; evidence for H2O and F open system behavior in melt inclusions, *Earth and Planetary Science Letters*, *287*(3–4), 442-452.
Maclennan, J. (2017), Bubble formation and decrepitation control the CO2 content of olivine - hosted melt inclusions, *Geochemistry, Geophysics, Geosystems*, *18*(2), 597-616.
Maclennan, J., D. McKenzie, F. Hilton, K. Gronvöld, and N. Shimizu (2003), Geochemical variability in a single flow from northern Iceland, *Journal of Geophysical Research: Solid Earth*, *108*(B1).
Mangan, M., and T. Sisson (2000), Delayed, disequilibrium degassing in rhyolite magma: decompression experiments and implications for explosive volcanism, *Earth and Planetary Science Letters*, *183*(3), 441-455.
Marty, B., T. Trull, P. Lussiez, I. Basile, and J.-C. Tanguy (1994), He, Ar, O, Sr and Nd isotope constraints on the origin and evolution of Mount Etna magmatism, *Earth and Planetary Science Letters*, *126*(1-3), 23-39.
Marziano, G. I., F. Gaillard, and M. Pichavant (2008), Limestone assimilation by basaltic magmas: an experimental re-assessment and application to Italian volcanoes, *Contr. Mineral. and Petrol.*, *155*(6), 719-738.
Mason, E., M. Edmonds, and A. V. Turchyn (2017), Remobilization of crustal carbon may dominate volcanic arc emissions, *Science*, *357*(6348), 290-294.
Matthews, S., O. Shorttle, J. F. Rudge, and J. Maclennan (2017), Constraining mantle carbon: CO 2-trace element systematics in basalts and the roles of magma mixing and degassing, *Earth and Planetary Science Letters*, *480*, 1-14.
McDonough, W. F., and S.-S. Sun (1995), The composition of the Earth, *Chemical geology*, *120*(3-4), 223-253.

Metrich, N., and R. Clocchiatti (1989), Melt inclusion investigation of the volatile behaviour in historic alkali basaltic magmas of Etna, *Bull Volcanol*, *51*(3), 185-198.
Metrich, N., and R. Clocchiatti (1996), Sulfur abundance and its speciation in oxidized alkaline melts, *Geochimica et Cosmochimica Acta*, *60*(21), 4151-4160.
Métrich, N., and P. J. Wallace (2008), Volatile Abundances in Basaltic Magmas and Their Degassing Paths Tracked by Melt Inclusions, *Reviews in Mineralogy and Geochemistry*, *69*(1), 363-402.
Métrich, N., P. Allard, N. Spilliaert, D. Andronico, and M. Burton (2004), 2001 flank eruption of the alkali-and volatile-rich primitive basalt responsible for Mount Etna's evolution in the last three decades, *Earth and Planetary Science Letters*, *228*(1), 1-17.
Michaud, V. (1995), Crustal xenoliths in recent hawaiites from Mount Etna, Italy: evidence for alkali exchanges during magma-wall rock interaction, *Chemical Geology*, *122*(1-4), 21-42.
Mollo, S., M. Gaeta, C. Freda, T. Di Rocco, V. Misiti, and P. Scarlato (2010), Carbonate assimilation in magmas: a reappraisal based on experimental petrology, *Lithos*, *114*(3-4), 503-514.
Montelli, R., G. Nolet, F. Dahlen, and G. Masters (2006), A catalogue of deep mantle plumes: New results from finite‐frequency tomography, *Geochemistry, Geophysics, Geosystems*, *7*(11).
Moore, G. (2008), Interpreting H2O and CO2 contents in melt inclusions: constraints from solubility experiments and modeling, *Reviews in Mineralogy and Geochemistry*, *69*(1), 333-362.
Mulas, M., R. Cioni, D. Andronico, and F. Mundula (2016), The explosive activity of the 1669 Monti Rossi eruption at Mt. Etna (Italy), *Journal of Volcanology and Geothermal Research*, *328*, 115-133.
Neave, D. A., J. Maclennan, M. Edmonds, and T. Thordarson (2014), Melt mixing causes negative correlation of trace element enrichment and CO< sub> 2</sub> content prior to an Icelandic eruption, *Earth and Planetary Science Letters*, *400*, 272-283.
Newman, S., and J. B. Lowenstern (2002), VolatileCalc: a silicate melt–H2O–CO2 solution model written in Visual Basic for excel, *Computers & Geosciences*, *28*(5), 597-604.
Patanè, D., G. Barberi, O. Cocina, P. De Gori, and C. Chiarabba (2006), Time-resolved seismic tomography detects magma intrusions at Mount Etna, *Science*, *313*(5788), 821-823.
Patanè, D., E. Privitera, S. Gresta, S. Alparone, A. Akinci, G. Barberi, L. Chiaraluce, O. Cocina, S. D'amico, and P. De Gori (2003), Seismological constraints for the dyke emplacement of the July-August 2001 lateral eruption at Mt. Etna volcano, Italy, *Annals of geophysics*.
Pedley, H. M., and M. Grasso (1992), Miocene syntectonic sedimentation along the western margins of the Hyblean-Malta platform: a guide to plate margin processes in the central Mediterranean, *Journal of Geodynamics*, *15*(1-2), 19-37.
Pichavant, M., I. Di Carlo, Y. Le Gac, S. G. Rotolo, and B. Scaillet (2009), Experimental constraints on the deep magma feeding system at Stromboli volcano, Italy, *Journal of Petrology*, *50*(4), 601-624.
Pichavant, M., I. Di Carlo, S. G. Rotolo, B. Scaillet, A. Burgisser, N. Le Gall, and C. Martel (2013), Generation of CO2-rich melts during basalt magma ascent and degassing, *Contr. Mineral. and Petrol.*, 1-17.
Roeder, P. L., and R. F. Emslie (1970), Olivine-liquid equilibrium, *Contr. Mineral. and Petrol.*, *29*(4), 275-289.
Ryan, W. B., S. M. Carbotte, J. O. Coplan, S. O'Hara, A. Melkonian, R. Arko, R. A. Weissel, V. Ferrini, A. Goodwillie, and F. Nitsche (2009), Global multi‐resolution topography synthesis, *Geochemistry, Geophysics, Geosystems*, *10*(3).

1022 Saal, A. E., E. H. Hauri, C. H. Langmuir, and M. R. Perfit (2002), Vapour undersaturation in
1023 primitive mid-ocean-ridge basalt and the volatile content of Earth's upper mantle, *Nature*,
1024 *419*(6906), 451-455.
1025 Schiano, P., R. Clocchiatti, L. Ottolini, and T. Busa (2001), Transition of Mount Etna lavas
1026 from a mantle-plume to an island-arc magmatic source, *Nature*, *412*(6850), 900-904.
1027 Schiavi, F., A. Rosciglione, H. Kitagawa, K. Kobayashi, E. Nakamura, P. M. Nuccio, L.
1028 Ottolini, A. Paonita, and R. Vannucci (2015), Geochemical heterogeneities in magma
1029 beneath Mount Etna recorded by 2001–2006 melt inclusions, *Geochemistry, Geophysics,*
1030 *Geosystems*, *16*(7), 2109-2126.
1031 Schobben, M., B. van de Schootbrugge, and P. B. Wignall (2019), Interpreting the carbon
1032 isotope record of mass extinctions, *Elements*.
1033 Shaw, A. M., M. D. Behn, S. E. Humphris, R. A. Sohn, and P. M. Gregg (2010), Deep
1034 pooling of low degree melts and volatile fluxes at the 85 E segment of the Gakkel Ridge:
1035 Evidence from olivine-hosted melt inclusions and glasses, *Earth and Planetary Science*
1036 *Letters*, *289*(3), 311-322.
1037 Shishkina, T. A., R. E. Botcharnikov, F. Holtz, R. R. Almeev, A. M. Jazwa, and A. A.
1038 Jakubiak (2014), Compositional and pressure effects on the solubility of H2O and CO2 in
1039 mafic melts, *Chemical Geology*, *388*, 112-129.
1040 Sides, I. R., M. Edmonds, J. Maclennan, D. A. Swanson, and B. F. Houghton (2014),
1041 Eruption style at Kīlauea Volcano in Hawai`i linked to primary melt composition *Nature*
1042 *Geoscience*, *7*, 464–469.
1043 Sobolev, A., and I. Nikogosian (1994), Petrology of long-lived mantle plume magmatism:
1044 Hawaii, Pacific and Reunion Island, Indian Ocean, *Petrology*, *2*(2), 111-144.
1045 Sobolev, A. V., A. W. Hofmann, and I. K. Nikogosian (2000), Recycled oceanic crust
1046 observed in 'ghost plagioclase'within the source of Mauna Loa lavas, *Nature*, *404*(6781),
1047 986-990.
1048 Soule, S. A., D. S. Nakata, D. J. Fornari, A. T. Fundis, M. R. Perfit, and M. D. Kurz (2012),
1049 CO2 variability in mid-ocean ridge basalts from syn-emplacement degassing: Constraints on
1050 eruption dynamics, *Earth and Planetary Science Letters*, *327–328*(0), 39-49.
1051 Spilliaert, N., N. Métrich, and P. Allard (2006a), S–Cl–F degassing pattern of water-rich
1052 alkali basalt: modelling and relationship with eruption styles on Mount Etna volcano, *Earth*
1053 *and Planetary Science Letters*, *248*(3), 772-786.
1054 Spilliaert, N., P. Allard, N. Métrich, and A. Sobolev (2006b), Melt inclusion record of the
1055 conditions of ascent, degassing, and extrusion of volatile‐rich alkali basalt during the
1056 powerful 2002 flank eruption of Mount Etna (Italy), *Journal of Geophysical Research: Solid*
1057 *Earth (1978–2012)*, *111*(B4).
1058 Tanguy, J., and G. Kieffer (1977), The 1974 eruption of Mount Etna, *Bulletin*
1059 *Volcanologique*, *40*(4), 239-252.
1060 Tanguy, J., G. Kieffer, and G. Patanè (1996), Dynamics, lava volume and effusion rate
1061 during the 1991–1993 eruption of Mount Etna, *Journal of Volcanology and Geothermal*
1062 *Research*, *71*(2-4), 259-265.
1063 Tanguy, J.-C., M. Condomines, and G. Kieffer (1997), Evolution of the Mount Etna magma:
1064 constraints on the present feeding system and eruptive mechanism, *Journal of Volcanology*
1065 *and Geothermal research*, *75*(3), 221-250.
1066 Venezky, D., and M. Rutherford (1997), Preeruption conditions and timing of dacite‐
1067 andesite magma mixing in the 2.2 ka eruption at Mount Rainier, *Journal of Geophysical*
1068 *Research: Solid Earth*, *102*(B9), 20069-20086.
1069 Viccaro, M., and R. Cristofolini (2008), Nature of mantle heterogeneity and its role in the
1070 short-term geochemical and volcanological evolution of Mt. Etna (Italy), *Lithos*, *105*(3), 272-
1071 288.

Viccaro, M., C. Ferlito, L. Cortesogno, R. Cristofolini, and L. Gaggero (2006), Magma mixing during the 2001 event at Mount Etna (Italy): effects on the eruptive dynamics, *Journal of Volcanology and Geothermal Research*, *149*(1), 139-159.
Wallace, P. J., V. S. Kamenetsky, and P. Cervantes (2015), Melt inclusion CO2 contents, pressures of olivine crystallization, and the problem of shrinkage bubbles, *American Mineralogist*, *100*(4), 787-794.
Witham, F., J. Blundy, S. C. Kohn, P. Lesne, J. Dixon, S. V. Churakov, and R. Botcharnikov (2012), SolEx: A model for mixed COHSCl-volatile solubilities and exsolved gas compositions in basalt, *Computers & Geosciences*, *45*, 87-97.
Woods, A. W., and S. S. Cardoso (1997), Triggering basaltic volcanic eruptions by bubble-melt separation, *Nature*, *385*(6616), 518.
Workman, R. K., E. Hauri, S. R. Hart, J. Wang, and J. Blusztajn (2006), Volatile and trace elements in basaltic glasses from Samoa: Implications for water distribution in the mantle, *Earth and Planetary Science Letters*, *241*(3–4), 932-951.
Zajacz, Z. (2015), The effect of melt composition on the partitioning of oxidized sulfur between silicate melts and magmatic volatiles, *Geochimica et Cosmochimica Acta*, *158*, 223-244.

Figure captions

Figure 1: Map of Mt. Etna with 1669 Monti Rossi scoria cone indicated. Lava flows from Monti Rossi cone to Catania are indicated in red from [*Branca et al.*, 2013] and sample sites at Monti Rossi cone are shown by black stars (SW and NE sides of cone). Map produced using *Geomapapp* (http://www.geomapapp.org) using the Global Multi-Resolution Topography (GMRT) Synthesis [*Ryan et al.*, 2009].

Figure 2: Photomicrographs of olivine crystals with melt inclusions (MI), oxide inclusions and matrix glass in samples: A: NEMR 67, B: SWMR 25, C: NEMR 141, D: NEMR 10. 500 m scale bar marked.

Figure 3: Major element oxide (wt. %) compositions for A.D. 1669 MI and MG (this study) compared to (i) 3930±60 B.P. (4 kyear) Fall-Stratified basalts (FS) MI [*Kamenetsky et al.*, 2007]; (ii) previous A.D. 1669 MI study [*Clocchiatti and Metrich*, 1984] (iii) A.D. 1669 WR lavas [*Corsaro et al.*, 1996]; (iv) 2002 MI [*Spilliaert et al.*, 2006b]; (v) 2001, 2002, 2006 MI [*Schiavi et al.*, 2015]. Symbols define different studies. The dashed line represents the modeled fractional crystallization path using the two end-member primitive FS melts at 1 kbar (solid line) and 4 kbar (dashed line) with Petrolog3 software [*Danyushevsky and Plechov*, 2011b]. Color bar scales for Ce/Y, a measure of degree of LREE-enrichment. Vectors represent assimilation of contaminants (Carbonate - C, Plagioclase - P, Gabbro - G)

1111 by the two end-member FS melts, adapted from [*Carter and Dasgupta*, 2015; *Mollo et al.*,
1112 2010].
1113
1114 **Figure 4**: Trace element profile for this study of A.D. 1669 melt inclusions (MI: fine gray
1115 line), 1669 matrix glass (MG: black dashed lines) compared to (i) 3930±60 B.P. Fall
1116 Stratified (FS) eruption MI (blue line; [*Kamenetsky et al.*, 2007]) and (ii) 2004, 2006, 2007
1117 eruption MI (coloured circles; [*Collins et al.*, 2009]). All concentrations are normalised to
1118 primitive mantle [*McDonough and Sun*, 1995].
1119
1120 **Figure 5**: (a) Nd and La trace element concentrations (ppm) for A.D. 1669 MI (this study)
1121 compared to (i) 3930 60 B.P. Fall-Stratified basalts (FS) MI [*Kamenetsky et al.*, 2007]; (ii)
1122 2001-2006 MI [*Schiavi et al.*, 2015]. Symbols as before. Solid black line represents modeled
1123 fractional crystallization (FC) path using two end-member primitive FS MI at 1 kbar and
1124 Petrolog3 software [*Danyushevsky and Plechov*, 2011a]. Color bars scale for Ce/Y, a
1125 measure of degree of LREE-enrichment: A.D. 1669 and FS: red-yellow, 2001-2006: gray-
1126 scale. (b) Ce against Y (ppm) for the same MI studies as (a) with gray lines of constant Ce/Y
1127 ratio and solid black lines as before. (c) La against Sr for 1669 MI showing negative
1128 correlation between Sr and LREE. (d) Sr against MgO showing breadth of Sr concentration in
1129 A.D. 1669 samples at a limited MgO wt.%. Solid black line as before.
1130
1131 **Figure 6**: (a) H_2O against CO_2 with closed (dotted lines) system degassing modeled from
1132 primitive FS melt compositions using SolEx [*Witham et al.*, 2012]. Isobars marked (SolEx)
1133 for both FS conditions (sold black line) and 1669 conditions (solid gray line). Symbols as
1134 before for A.D. 1669 MI and MG (this study), 2002 MI [*Spilliaert et al.*, 2006b] and FS
1135 [*Kamenetsky et al.*, 2007] MI. (b) Positive correlation of CO_2 against sulfur in 1669 MI.
1136 Symbols and colour bar as before. (c) Negative correlation of CO_2 against Nb in 1669 MI and
1137 MG. Symbols and colour bar as before. FS MI do not follow the same correlation. (d)
1138 Positive correlation of CO_2 against Sr anomaly (Sr/Sr*). Sr* calculated from the relative
1139 compatibility of neighboring REE Ce and Nd, see text for details of calculation.
1140
1141 **Figure 7**: Model of possible mechanisms to account for Sr-rich, CO_2-rich depleted melts
1142 mixing with Sr-poor, CO_2-poor enriched melts in the shallow crust. MI symbols for 1669, FS
1143 and 2001, 2002, 2006 same as before. Fractional crystallization (FC) of FS-melt modeled by
1144 Petrolog3 software [*Danyushevsky and Plechov*, 2011a] indicated by vertical arrows. (a)

Model of mantle melting: (i) KG1(8) pyroxenite melting at F=0.01 accumulated fractions (turquoise), ticks mark degree of melting. (ii) KLB-1 peridotite melting at F=0.01 accumulated fractions (dark blue line), ticks mark degree of melting. (b) Models of contaminant assimilation: (i) plagioclase (blue line) assimilation: ticks mark fraction of contaminant mixed into depleted and enriched FS-melts and blue arrows signify 70% FC of the end-member melts after 30% contamination by plagioclase; (ii) 10% gabbro melt (pink line) assimilation: ticks mark fraction of contaminant mixed into enriched FS-melts. Pink box 1 is the whole rock (WR) composition of the AMLG gabbro [*Corsaro et al.*, 2014] and box 2 is the composition of the 10% batch melt from this gabbro (iii) carbonate (green line) assimilation, ticks mark fraction of contaminant mixed into LREE-enriched and LREE-depleted FS-melt. Green box is the composition of Etnean carbonate xenolith contaminant. The green arrows signify 70% FC of the LREE-enriched melt after 0% carbonate assimilation (i), and 50% carbonate assimilation (ii).

Figure 8: a) Melt inclusion CO_2 concentrations plotted against Ce/Y for both 1669 melts (orange triangles) and FS melts (red circles); b) Saturation pressures calculated using major element parameterization [*Shishkina et al.*, 2014], which takes into the account the variable CaO and alkali contents of the end member melts, plotted against Ce/Y.

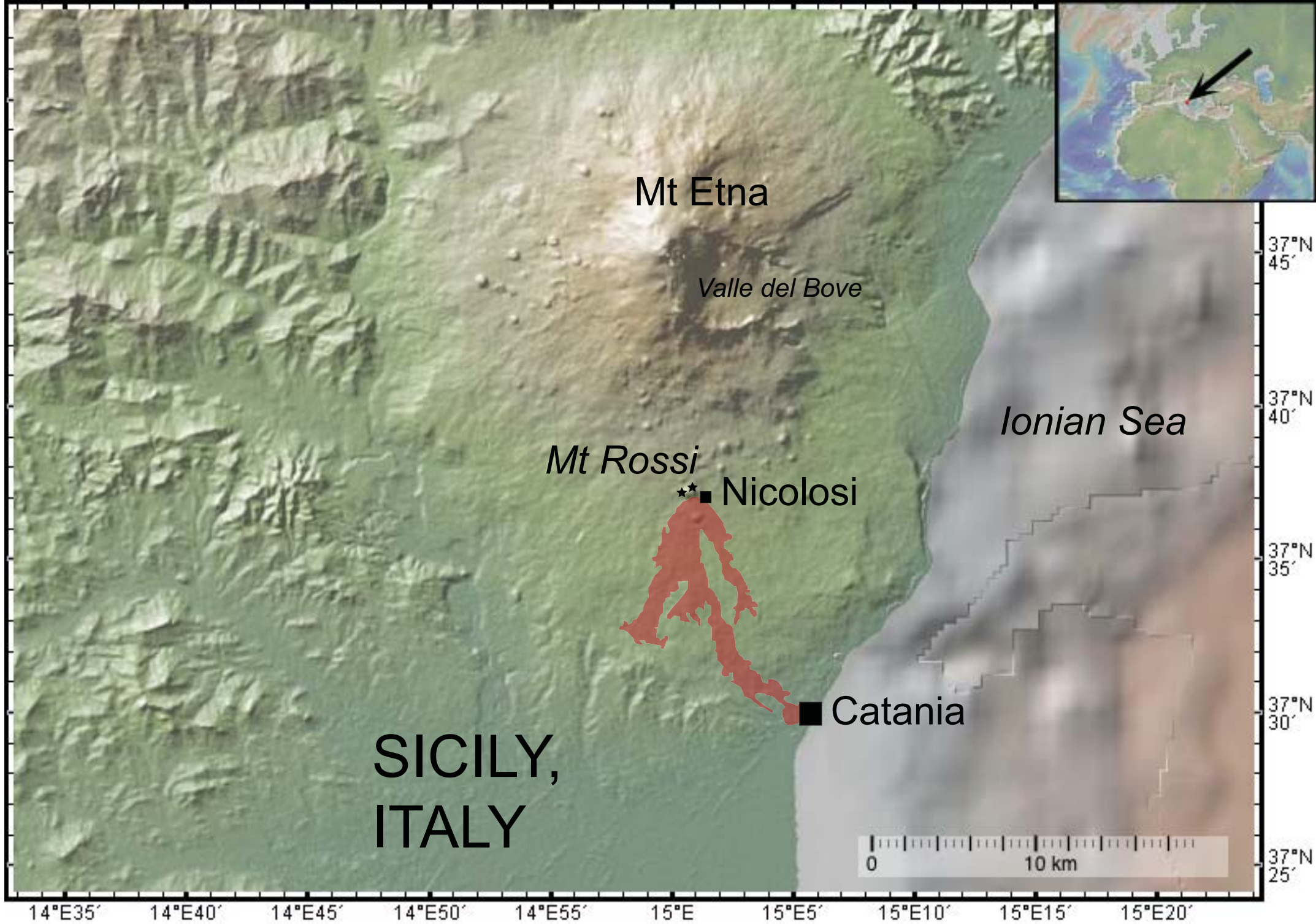
Mt Etna
Valle del Bove
Ionian Sea
Mt Rossi
Nicolosi
Catania
SICILY,
ITALY
0
10 km
37°N 45′
37°N 40′
37°N 35′
37°N 30′
37°N 25′
14°E35′
14°E40′
14°E45′
14°E50′
14°E55′
15°E
15°E5′
15°E10′
15°E15′
15°E20′

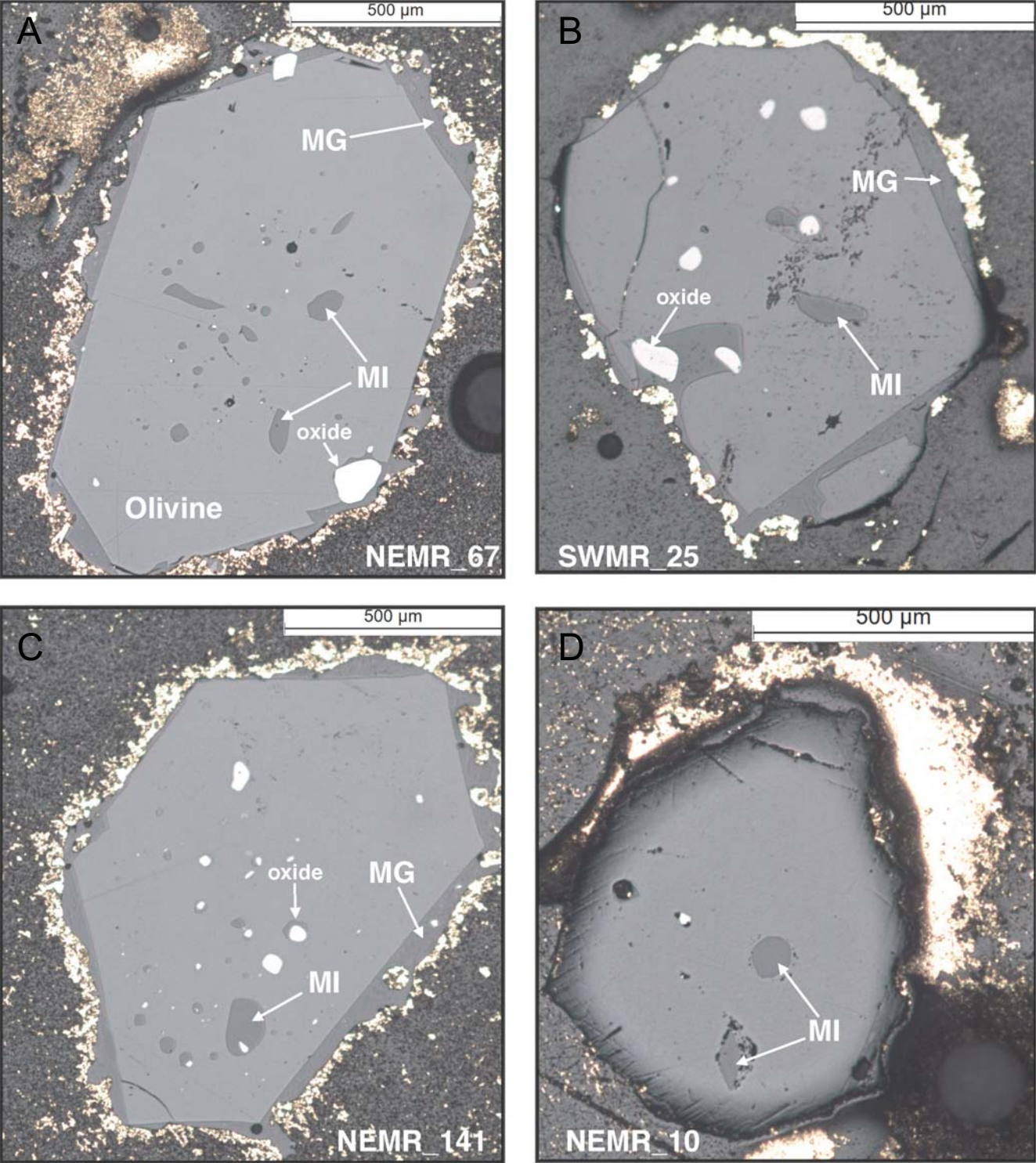
A
500 µm
MG
MI
oxide
Olivine
NEMR_67
B
500 µm
MG
oxide
MI
SWMR_25
C
500 µm
oxide
MG
MI
NEMR_141
D
500 µm
MI
NEMR_10

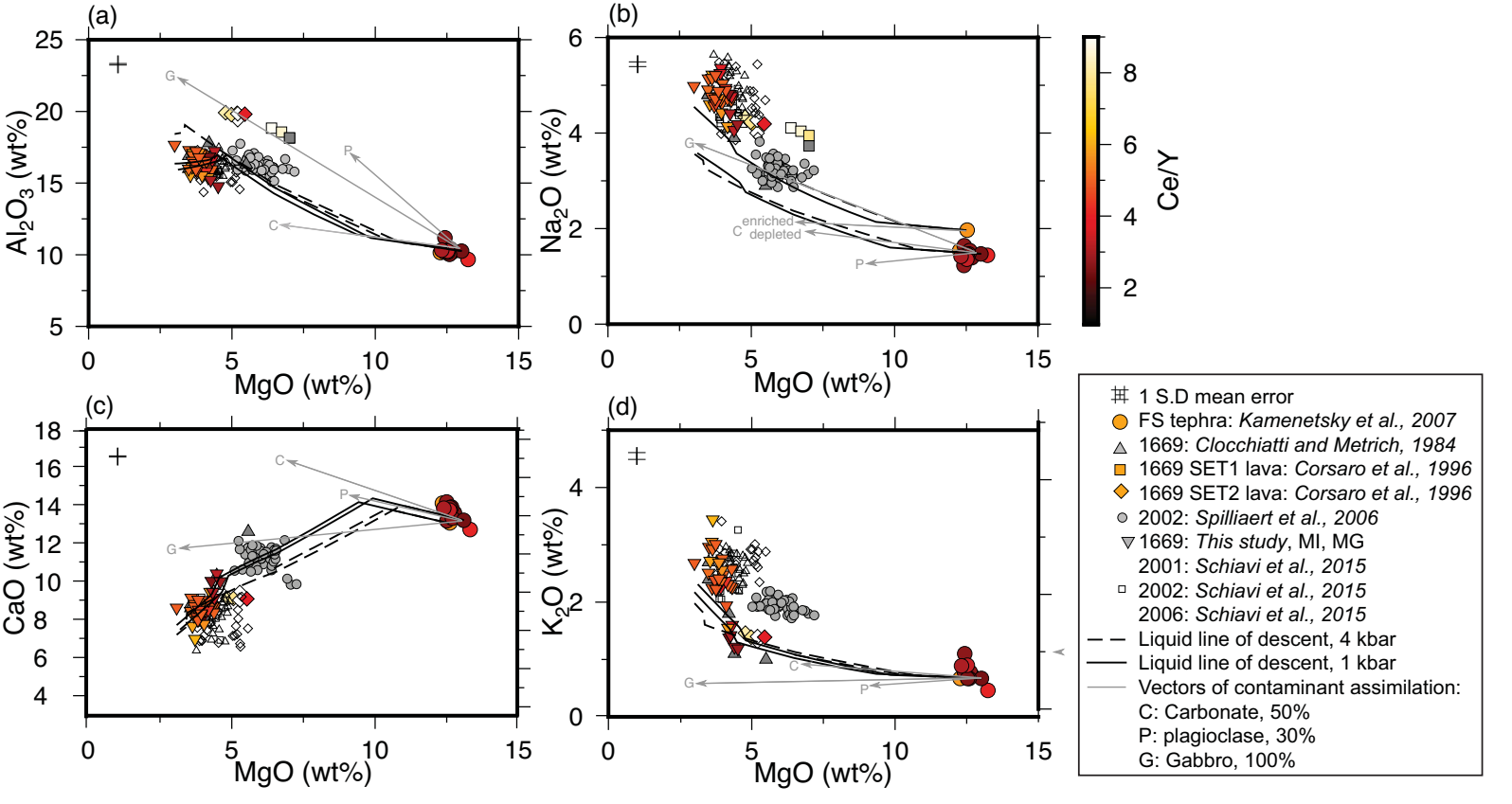
(a)
(b)
(c)
(d)
Al_2O_3 (wt%)
Na_2O (wt%)
CaO (wt%)
K_2O (wt%)
MgO (wt%)
Ce/Y
G
P
C
enriched
depleted
1 S.D mean error
FS tephra: Kamenetsky et al., 2007
1669: Clocchiatti and Metrich, 1984
1669 SET1 lava: Corsaro et al., 1996
1669 SET2 lava: Corsaro et al., 1996
2002: Spilliaert et al., 2006
1669: This study, MI, MG
2001: Schiavi et al., 2015
2002: Schiavi et al., 2015
2006: Schiavi et al., 2015
Liquid line of descent, 4 kbar
Liquid line of descent, 1 kbar
Vectors of contaminant assimilation:
C: Carbonate, 50%
P: plagioclase, 30%
G: Gabbro, 100%

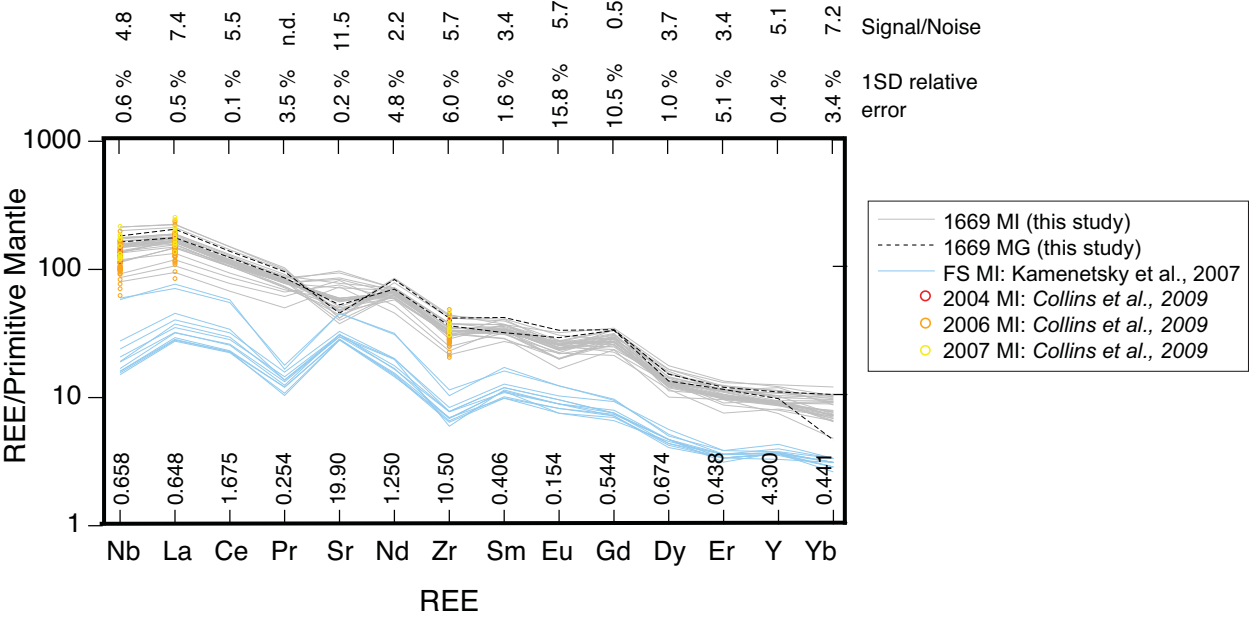
Signal/Noise
4.8
7.4
5.5
n.d.
11.5
2.2
5.7
3.4
5.7
0.5
3.7
3.4
5.1
7.2
1SD relative error
0.6 %
0.5 %
0.1 %
3.5 %
0.2 %
4.8 %
6.0 %
1.6 %
15.8 %
10.5 %
1.0 %
5.1 %
0.4 %
3.4 %
1669 MI (this study)
1669 MG (this study)
FS MI: Kamenetsky et al., 2007
2004 MI: Collins et al., 2009
2006 MI: Collins et al., 2009
2007 MI: Collins et al., 2009
REE/Primitive Mantle
1000
100
10
1
0.658
0.648
1.675
0.254
19.90
1.250
10.50
0.406
0.154
0.544
0.674
0.438
4.300
0.441
Nb
La
Ce
Pr
Sr
Nd
Zr
Sm
Eu
Gd
Dy
Er
Y
Yb
REE

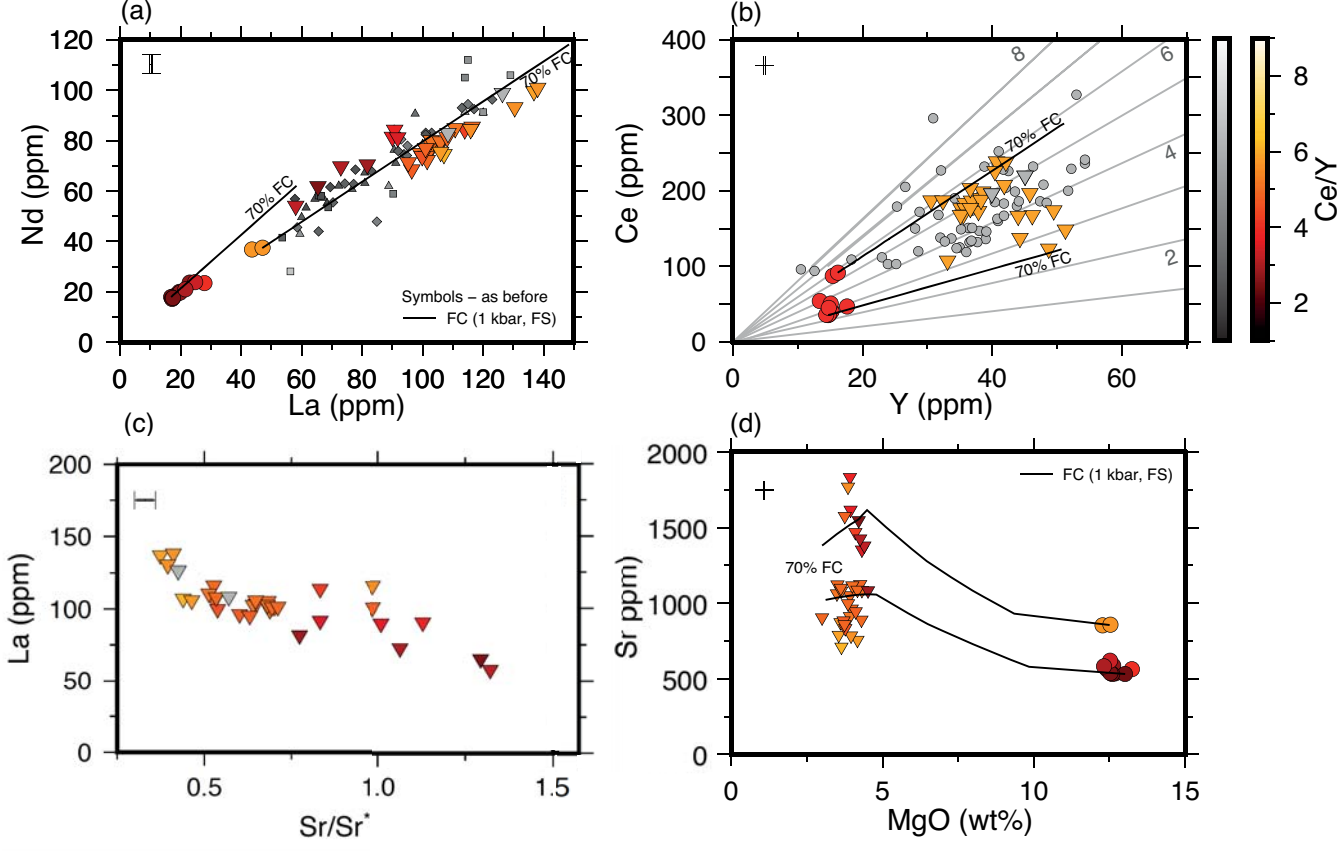
(a)
Nd (ppm)
La (ppm)
70% FC
70% FC
Symbols – as before
FC (1 kbar, FS)
(b)
Ce (ppm)
Y (ppm)
8
6
4
2
70% FC
70% FC
Ce/Y
(c)
La (ppm)
Sr/Sr*
(d)
Sr ppm)
MgO (wt%)
FC (1 kbar, FS)
70% FC

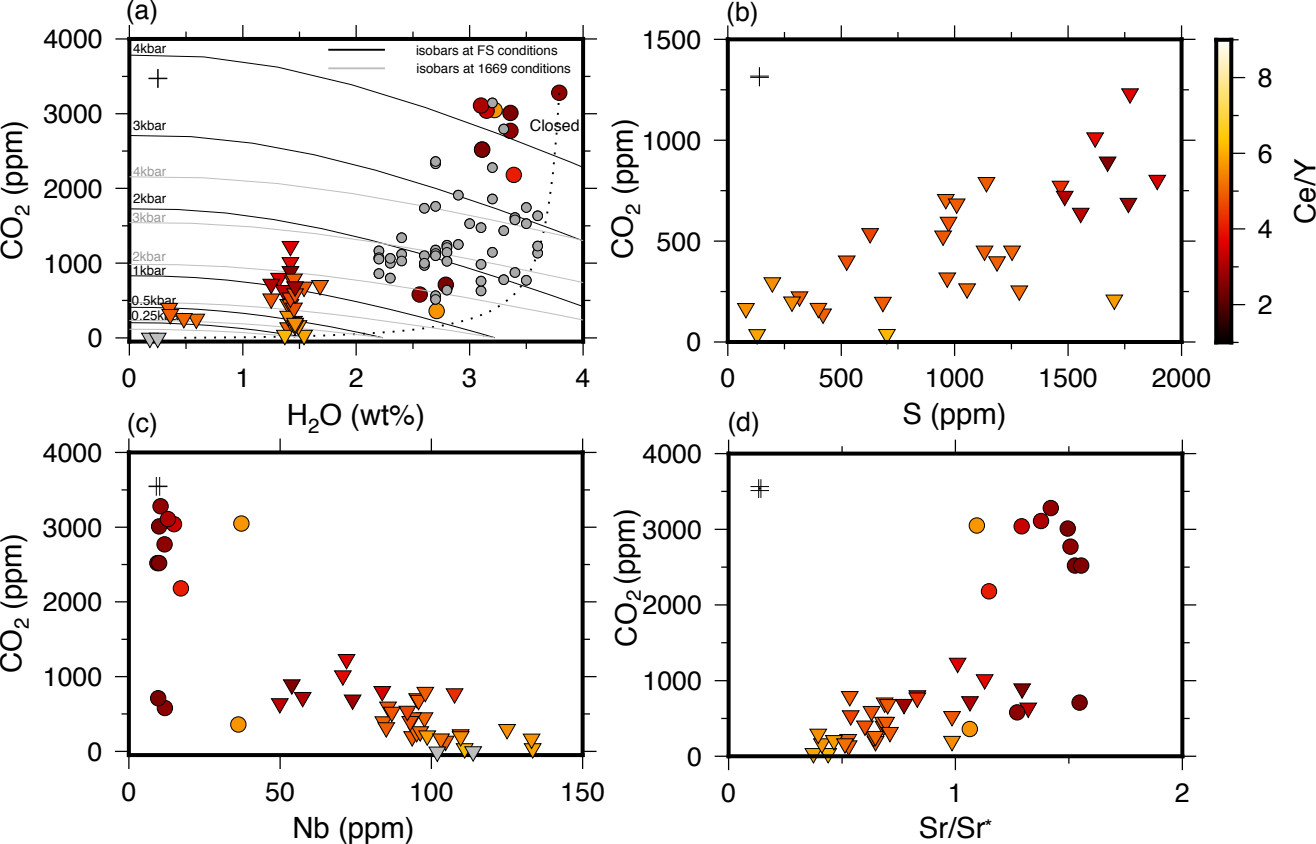
(a)
4kbar
3kbar
4kbar
2kbar
3kbar
2kbar
1kbar
0.5kbar
0.25kb
isobars at FS conditions
isobars at 1669 conditions
Closed
CO2 (ppm)
H2O (wt%)
(b)
CO2 (ppm)
S (ppm)
Ce/Y
(c)
CO2 (ppm)
Nb (ppm)
(d)
CO2 (ppm)
Sr/Sr*

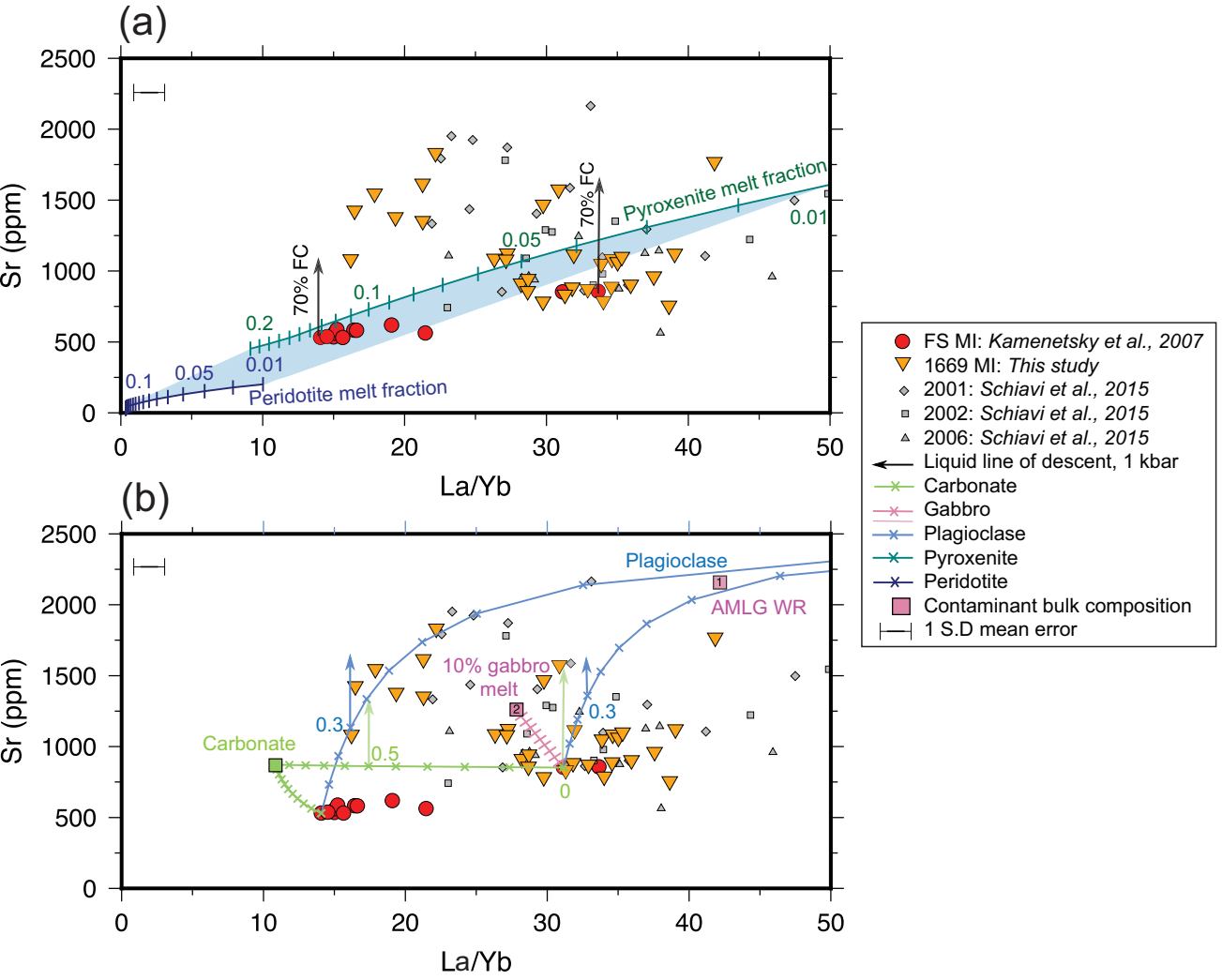
(a)
Sr (ppm)
La/Yb
70% FC
70% FC
Pyroxenite melt fraction
Peridotite melt fraction
0.2
0.1
0.05
0.01
0.1
0.05
0.01
(b)
Plagioclase
AMLG WR
10% gabbro melt
Carbonate
0.3
0.5
0.3
0
FS MI: Kamenetsky et al., 2007
1669 MI: This study
2001: Schiavi et al., 2015
2002: Schiavi et al., 2015
2006: Schiavi et al., 2015
Liquid line of descent, 1 kbar
Carbonate
Gabbro
Plagioclase
Pyroxenite
Peridotite
Contaminant bulk composition
1 S.D mean error

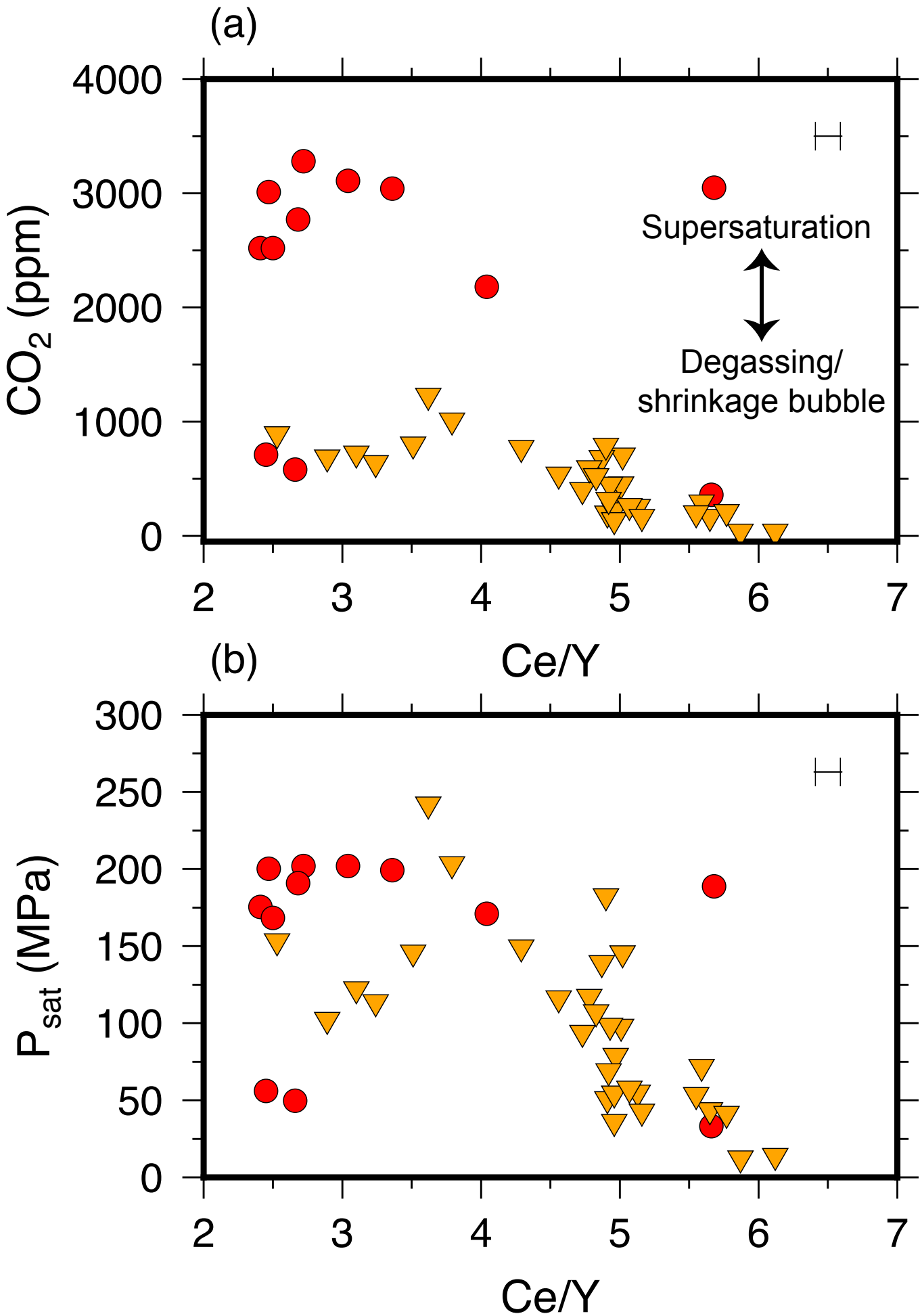
(a)
4000
3000
2000
1000
0
CO_2 (ppm)
Supersaturation
Degassing/
shrinkage bubble
2
3
4
5
6
7
Ce/Y
(b)
300
250
200
150
100
50
0
P_{sat} (MPa)
2
3
4
5
6
7
Ce/Y

Supporting Information for "Carbon dioxide in geochemically heterogeneous melt inclusions from Mount Etna, Italy"

L. C. Salem,[1], M. Edmonds[1], R. A. Corsaro,[2] and J. Maclennan[1]

Contents of this file

1. Text S1 to S4
2. Figures S1 to S6
3. Tables S1 to S5

Corresponding author: Marie Edmonds, Department of Earth Sciences, University of Cambridge, Downing Street, Cambridge, CB2 3EQ, United Kingdom (marie.edmonds@esc.cam.ac.uk)

[1]Department of Earth Sciences,
University of Cambridge, Downing Street,
Cambridge, CB2 3EQ, United Kingdom

[2]Istituto Nazionale di Geofisica e
Vulcanologia, Sezione di Catania, Piazza
Roma 2, 95123 Catania, Italy

Introduction The following supplementary material supplies detailed methodological and analytical details in addition to those provided in the main manuscript text. Equations and methods used to model mantle melting are described in Sections S1, Analytical Techniques and conditions are described in Section S2 and S3. The Principle Component Analysis methodology is described in section S4. Data tables and supplementary figures are also included that support the manuscript and are referenced in the main text.

Melting equations and models S1 A batch melting equation [*Winter*, 2010] was used to model melting of the ALMG Etna gabbro [*Corsaro et al.*, 2014]. Let C_o be the trace element concentration of the original rock before melting, C_m be the trace element concentration of the melt, D_i be the bulk partition coefficient of element 'i' and F be the wt% fraction of melt produced

$$C_m = \frac{C_o}{Di(1-F)+F}, \tag{1}$$

Incremental fractional melting of KLB-1 peridotite [*Davis et al.*, 2009; *Jennings and Holland*, 2015] and KG1(8) pyroxenite [*Kogiso et al.*, 1998; *Jennings et al.*, 2016] at T_p 1315 °C and 1500 °C were modeled using the methods outlined in *Jennings and Holland* [2015] and *Jennings et al.* [2016] respectively. These models use P-T-F (pressure-temperature-melt fraction) pathways for decompression melting calculated assuming anhydrous and isentropic conditions according to the method of *Katz et al.* [2003]. The differential equation (provided by *Katz et al.* 2003, originally *McKenzie* 1984) for dF/dP is numerically integrated using a fourth-order RungeKutta scheme. For peridotite melting, the solidus, liquidus and melt productivity parametrization of *Katz et al.* [2003] were used, along with

the thermal properties of *Shorttle et al.* [2014]. For pyroxenite melting, the new solidus, liquidus and melt productivity parametrization of *Jennings et al.* [2016] for the KG1(8) composition was used. The parameters used are listed in Table A1 of *Jennings et al.* [2016] and the new thermodynamic model for calculating phase relations during mantle melting from 0.001 to 60 kbar and from 800 °C to liquidus temperatures in the system NCFMASOCr is outlined in *Jennings and Holland* [2015]. The trace elemental partition coefficients and bulk peridotite and pyroxenite compositions of *Stracke and Bourdon* [2009] were used in conjunction with the phase relations calculated by *Jennings et al.* [2016] and *Jennings and Holland* [2015] in order to compute the full trace element composition of the melt at each 0.01 fractional melt increment. Instantaneous 0.01 melt fractions were generated by the model and then accumulated to obtain the composition of melt fractions from 0 to 0.2.

Analytical Method: Secondary Ion Mass Spectrometry (SIMS) S2

All SIMS analyses were performed on a Cameca ims-4f instrument at the NERC Ion Microprobe Facility at the University of Edinburgh, UK in one analytical session in October 2013. Carbon (C) was measured separately from other volatiles and trace elements in the first round of analysis. When measuring C, the SIMS is configured with a high mass resolving power in order to ensure good separation of ^{12}C and $^{24}Mg^{2+}$ peaks. Other volatiles and trace elements were subsequently measured in a second round of analyses. SIMS measurements of C were the first measurements made on the samples. Samples were then C-coated and analyzed by EPMA after SIMS to prevent the risk of contamination from the C-coat. Measurements were made using a primary O^- ion beam with an accelerating voltage of 15 kV, a beam current of 5 nA, a secondary accelerating voltage of

4500 V minus a 50 V offset, to resolve the tail of the C-peak from the Mg^{2+} peak, and a 25 μm image field. The ion beam was rastered over an area of approximately 20 μm^2 for 180 seconds as a pre-sputter prior to analysis to remove surface contamination. The raster was then switched off and a 15 μm beam centered in the middle of the rastered area was used to make measurements. The following isotopes were measured for 15 cycles, with counting times in seconds in parentheses: $^{12}C(5)$, $^{24}Mg^{2+}(10)$, $^{28}Si^{2+}(2)$ and $^{30}Si(2)$. Only counts from the final 8 cycles, when count rates reach an asymptote and the effects of surface contamination are minimal, were retained to calculate C concentrations. A background correction was performed by subtracting the number of C counts measured using the CO_2-free standard BIR-1G [*Jochum et al.*, 2005]. C concentrations were calculated using a calibration curve constructed with a suite of basaltic glass standards (17-2, S5-14, S4-13, S2-3) of CO_2 content 0-3000 ppm [*Pichavant et al.*, 2009]. Accuracy expressed as % recovery of published compositions determined by Fourier-transform infrared spectroscopy (FTIR), was 100.6%. Precision was estimated as 1SD (σ) = 0.7% using 3 repeat analyses of each standard.

Water (H_2O), fluorine (F) and trace elements were measured as part of the same analysis set-up after C analyses had been completed. Measurements were made using a primary O^- ion beam with an accelerating voltage of 15 kV, a beam current of 5 nA, a secondary accelerating voltage of 4500 V minus a 75 V offset and a 25 μm image field. The ion beam was rastered over the same area as the C analysis but for 120 seconds. Analyses were made with a spot size of approximately 25 μm x 25 μm cantered in the pit made during the preceding C analysis. The following isotopes were measured for 10 cycles, with counting times in seconds in parentheses: $^{1}H(5)$, $^{19}F(5)$, $^{30}Si(2)$, $^{35}Cl(5)$, $^{47}Ti(3)$, $^{84}Sr(3)$, $^{88}Sr(3)$,$^{89}Y(3)$,

^{90}Zr(3), ^{93}Nb(3), atomic mass 130.5(3), ^{138}Ba(3), ^{139}La(3), ^{140}Ce(3), ^{141}Pr(5), ^{143}Nd(5), ^{149}Sm(8), ^{151}Eu(10), ^{138}BaO+^{154}Gd(5), ^{140}CeO+^{156}Gd(4), 157Gd(8), ^{159}Tb(5), ^{161}Dy(5), ^{165}Ho(5), ^{167}Er(8), ^{169}Tm(8), ^{171}Yb(10) and ^{175}Lu(10). Peak positions were verified before each analysis, and mass 130.5 was measured to determine the electron multiplier backgrounds in each cycle, which were always sufficiently close to zero to be ignored. The overlap of BaO on Eu was monitored using the mass 154 peak (^{138}BaO+^{154}Gd(5) and the overlap of the light REE, Gd and Tb oxides, on the heavy REE by use of mass 156 (^{140}CeO+^{156}Gd(4)) Only the first 5 or 6 cycles of each 10 cycles of analyses were used due to mass drift. H_2O concentrations were calculated using a calibration curve constructed with 17-2, S2-3 and S5-14 glass standards with H_2O contents of 4.82, 3.15 and 3.46 wt.% respectively *Pichavant et al.* [2009]. Accuracy expressed as % recovery of published compositions determined by Fourier-transform infrared spectroscopy (FTIR), was 100.6%. Precision was estimated as 1SD = 1.1% using 3 repeat analyses of 17-2 and S2-3. Drift was monitored using repeat analyses of 17-2 and S2-3 at the start, middle and end of each day. 2-7% drift in calculated H_2O concentrations was observed on three days of H_2O data collection and a linear correction was made. F concentrations were calculated using a calibration curve constructed with the international standards NIST-610 and BCR-2G [*Jochum et al.*, 2005, 2011]. Accuracy was monitored by analysis of international standards NIST-610 and BCR-2G throughout analytical sessions. Average accuracy expressed as % recovery of published compositions determined by FTIR, was $> 70\%$ for all trace elements. Precision was estimated as 1σ relative error and varied between 0.1% (Ce) and 15.8% (Eu) using repeat analyses of BCR-2G [*Jochum et al.*, 2011]. Precision was calculated for trace element ratios and volatile/trace ratios using repeat

analyses of the same standards. 1 σ percentage relative error is in parentheses: La/Yb (0.5), Ce/Y (2.9), CO_2/Nb (0.9) and H_2O/Ce (1.1). Concentrations were calculated by normalizing ^{30}Si to Si determined subsequently by EMPA at the University of Cambridge. The following international standards were measured at the start of each day to monitor the calibration and drift: BCR-2G, BIR-1G and NIST-610 (Jochum et al., 2005, 2006). The trace element content of 17-2 and S2-3 was also monitored throughout each day to check for drift, though none was observed. Absolute element concentrations were calculated using JCION-6 software, where corrections were also made for oxide interferences of light REEs on the heavy REEs and BaO on Eu. The magnitude of oxide correction relates to the offset voltage at which the data are processed. Minor sample charging variations were checked (and corrected for) by use of the CeO/Ce ratio (based on the corrected mass ^{156}CeO/^{140}Ce ratio.

Analytical Method: Electron probe microanalysis (EPMA) S3 Major element compositions of macrocrysts, matrix glasses and melt inclusions were determined using a Cameca SX100 instrument at the University of Cambridge, UK. Glass analyses were performed with a spot size of 5 μm, an operating potential of 15 kV and a beam current of 6 nA. Olivine analyses were performed with a spot size of 1 μm, an operating potential of 15 kV and a beam current of 20 nA. Counting times were as follows for glass: Mg(80), Si(20), Fe(40), Ca(40), Al(80), Na(10), Ti(60), K(10), Mn(90), Cr(80), P(60), Cl(90), S(120), F(120), and for olivine: Mg(20), Si(20), Fe(20), Ca(60), Al(90), Ni(60), Ti(60), Mn(40), Cr(40), P(90). Calibration standards were as follows: jadeite for Na, periclase for Mg, Si glass for Si, K-feldspar for K, rutile for Ti, fayalite for Fe, corundum for Al, apatite for P, and pure metals for Cr, Mn and Ni. Data reduction was performed using

the inbuilt CamecaX-Phi PeakSight software for glass analyses and PAP corrections for mineral analyses. Most analyses returned totals of 98.5-101.5 wt.%. Samples with totals outside this range or with inappropriate stoichiometry were discarded. MgO content of the St. Johns Island Olivine standard was determined with a precision of 0.1(1SD) wt.% (n=13).

Principal Component Analysis (PCA) S4 [*Albar`ede*, 1996; *McKenzie and O'Nions*, 1998] is a method to extract uncorrelated variables from sets of data, to allow the main trends to be isolated. PCA analysis of the 1669 melt inclusion trace element compositions indicates that the first two principal components (PC1 principal component 1 with standard deviation 2.738 and PC2 principal component 2 with standard deviation 2.642) describe 50% of the variance in trace element dataset. Plotting PC1 and PC2 across the element array (Supplementary Figure S5) shows that PC1, which involves all trace elements behaving similarly (PC1) except Sr (PC1), highlights an anomaly in the behaviour of Sr. There is some variability in PC1 for the HREE with more compatible elements 0. If the process that is fractionating Sr from other elements results in its depletion in the melt, PC1 may be due to fractional crystallization of plagioclase; Sr is compatible in plagioclase while all other REE are incompatible and become enriched in the melt. However, if Sr is being enriched in the melt, PC1 may be due to assimilation of Sr from some source or contaminant, and this process may also affect the different PC1 scores of HREE compared to LREE. PC2 is positive for the LREE and negative for the HREE (Supplementary Figure S5) and this pattern of vectors could result from a variable primary melt composition (i.e. a melting signature). PC2 might be related to (1) the depth of melting and the presence of garnet in the melting region where HREE are compatible, (2) the

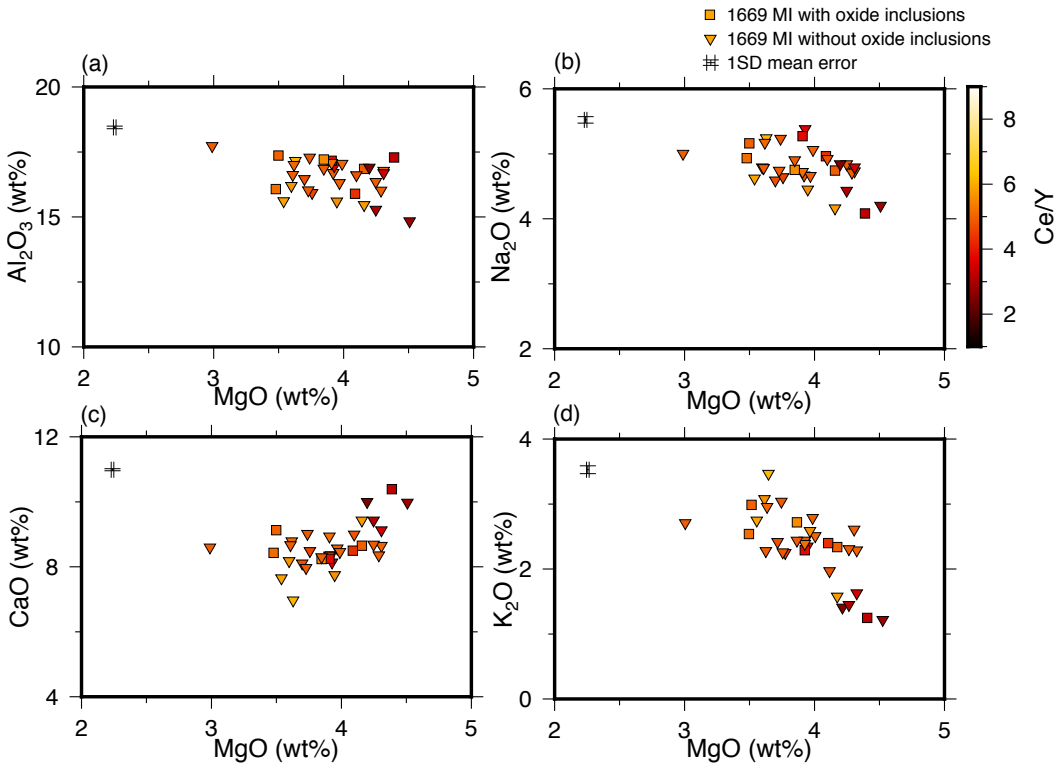

Figure S1. Major element oxide (wt.%) compositions for A.D. 1669 MI (this study) with daughter oxide inclusions (squares) and without trapped oxide inclusions (triangles). Color bar scales are for Ce/Y, a measure of degree of LREE-enrichment.

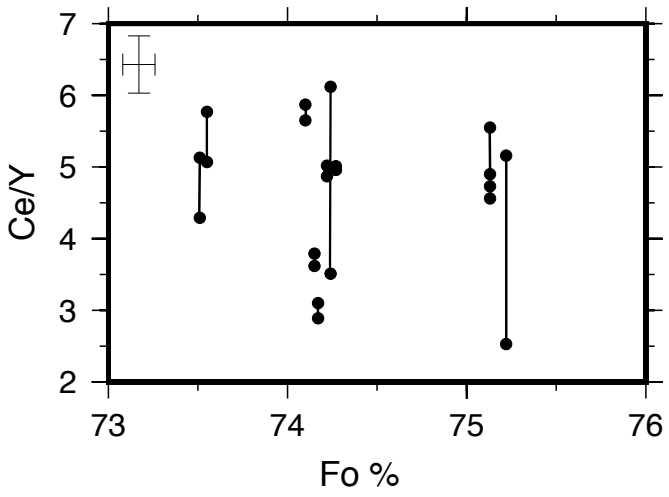

Figure S2. Host Fo composition against Ce/Y as a measure of LREE-enrichment for A.D. 1669 MI (this study). The black vertical lines join analyses of MI in the same olivine host crystal. The range of Ce/Y for each line indicates a lack of correlation between LREE-enrichment and Fo content.

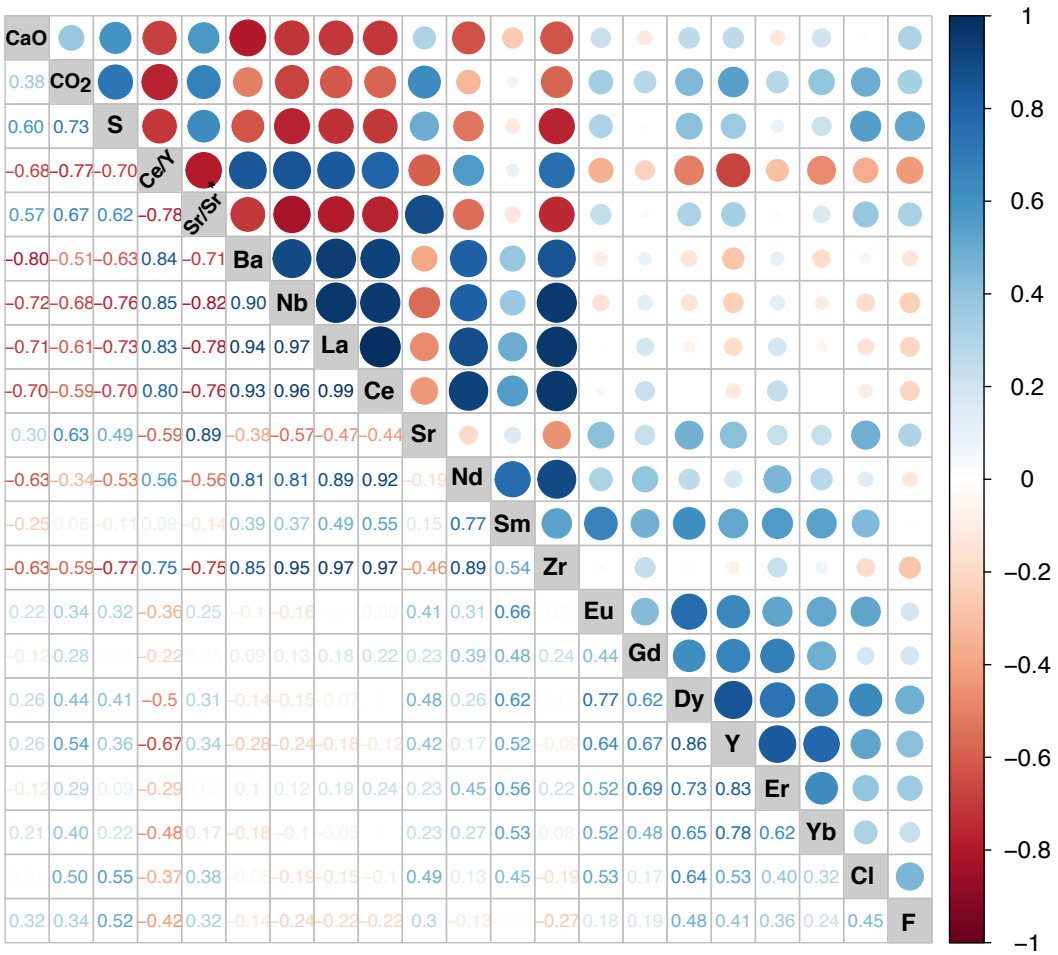

Figure S3. Cross-Correlation matrix generated by the corrplot package in R showing positive and negative correlation between species measured in MI. Blue symbols denote positive correlation and red, negative, the size of the symbol denotes the strength of the correlation. Larger symbols denote a stronger correlation. In the upper-right of the plot large dark symbols show strong correlations and small pale symbols, weak correlation. In the lower-left of the plot regression values (r) are shown and colored by the same scale.

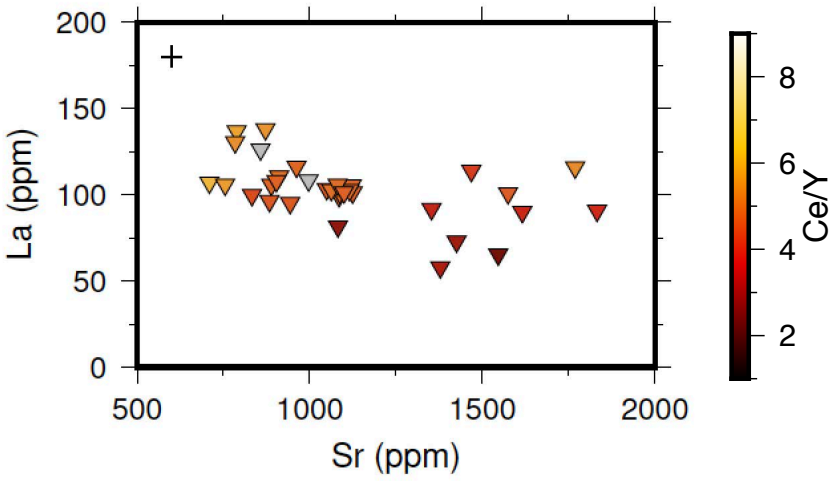

Figure S4. Negative correlation of La against Sr (ppm). Symbols and color bar as before.

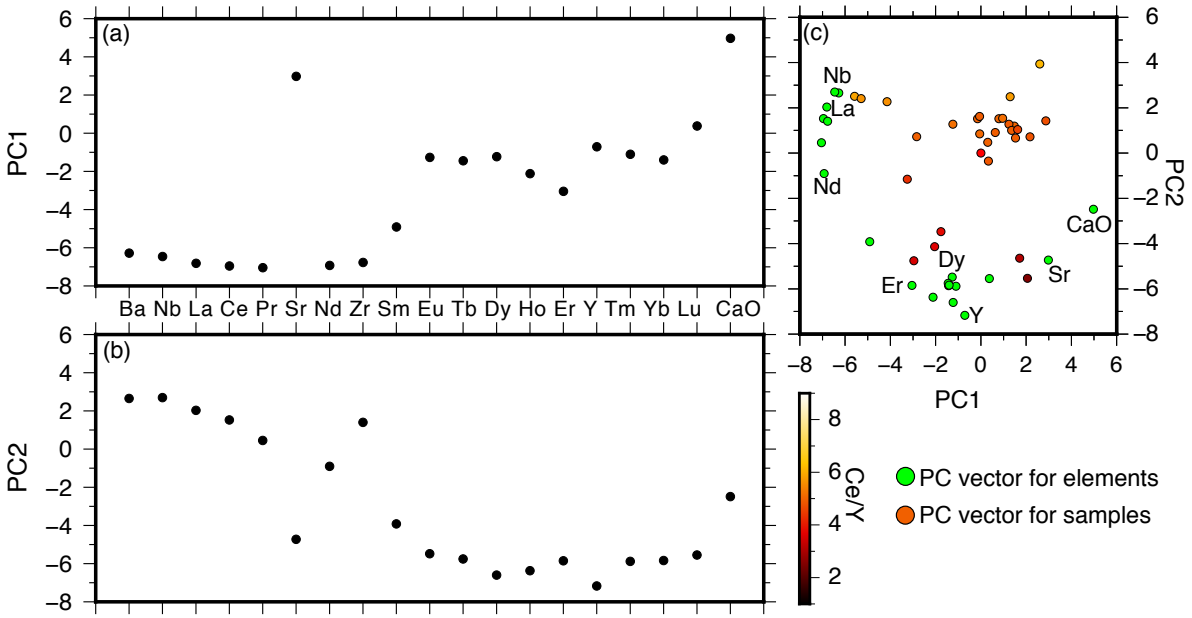

Figure S5. Principle Component Analysis of PC1 (a) and PC2 (b) for each element analyzed. (c) PC1 plotted against PC2 vectors for each MI analyzed, colored for degree of LREE/HREE enrichment (same as before). Vectors of PC1 and PC2 from (a) and (b) are also plotted and labeled by element (green circles).

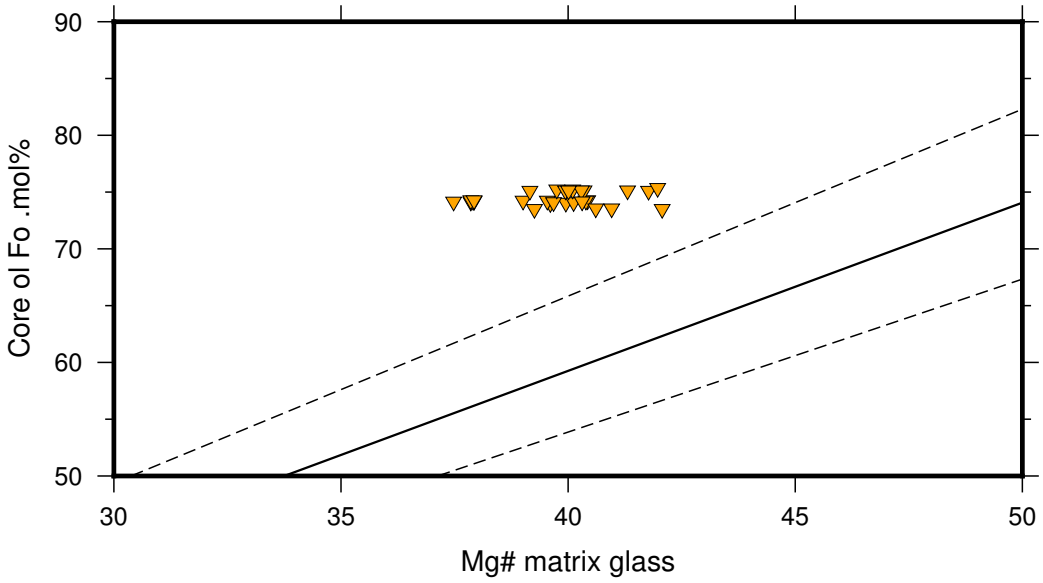

Figure S6. Rhodes plot of host olivine core Fo content against Mg# of the corresponding matrix glass for 1669 olivine crystals. Solid line represents $K_D = 0.3$, dashed lines ± 10%

Table S1. Summary of estimated accuracy and precision for all elements measured by EPMA and SIMS. Precision is expressed as 1σ percentage relative error (%P) and was calculated using [a]repeat analysis of basaltic glass standards by EPMA, [b]repeat analyses of standards NIST-610 and BCR-2G for trace elements [*Jochum et al.*, 2005, 2011], [b]repeat analyses of 17-2, S2-3 and S5-14 glass standards for H_2O [*Pichavant et al.*, 2009], and [b]repeat analyses of 17-2, S5-14, S4-13, S2-3 glass standards for CO_2 [*Pichavant et al.*, 2009]. [c]Accuracy is expressed as % recovery (A%) with respect to NIST-610 and BCR-2G standards [*Jochum et al.*, 2005] for trace elements and a range of standards with compositions given by *Shishkina et al.* [2010] and *Pichavant et al.* [2009] for CO_2 and H_2O.

Technique	EPMA	SIMS	SIMS
Element	%P[a] (MI)	%P[b] (MI)	%A[c] (MI)
SiO2	0.3		
TiO2	1.6		
Al2O3	0.9		
FeOt	1.2		
MnO	7.6		
MgO	0.7		
CaO	0.4		
Na_2O	2.9		
K_2O	4.8		
Cr_2O_3	55.8		
P_2O_5	3.6		
NiO	33.9		
S	1.0		
Cl	3.2		
F	33.2		
H_2O		1.1	100.6
CO_2		0.7	100.6
Sr		0.2	102.6
Y		0.4	108.9
Zr		1.6	115.6
Nb		0.6	106.3
Ba		0.1	105.6
La		0.5	100.9
Ce		0.1	101.2
Pr		2.5	104.9
Nd		4.8	99.0
Sm		6.0	98.0
Eu		15.8	98.5
Gd		10.5	102.6
Tb		3.5	103.0
Dy		1.0	102.0
Ho		9.3	102.5
Er		5.1	99.6
Tm		15.3	104.7
Yb		3.4	102.4
Lu		6.3	102.8

Table S2. Melt inclusions major, trace and volatile element data acquired by EPMA and SIMS with calculated trace element and voaltile ratios, Sr/Sr* and host olivine Fo mol.% for NEMR melt inclusions

MI Name	**NEMR** 10a	10b	26a	67a	67b	67c	76a	76b	80a	113a	113b	114a	126a	126b	140a	140b
SiO_2 wt.%	48.36	50.22	48.45	50.33	49.59	50.58	49.59	46.8	51.89	49.8	49.68	50.3	49.47	45.72	50.03	49.75
TiO_2	1.93	2.09	1.65	2.05	2.03	2.12	1.4	1.82	1.8	1.81	1.98	1.92	1.91	1.49	1.59	1.71
Al_2O_3	15.54	16.13	17.29	16.24	16.98	15.95	15.82	16	17.09	16.71	16.28	16.7	16.94	15.39	16.89	17.09
FeO_T	9.74	10.35	10.98	10.55	10.9	11	11.74	11.02	9.97	10.56	10.42	10.81	11.43	11.57	10.98	10.98
MnO	0.19	0.17	0.21	0.32	0.24	0.17	0.3	0.26	0.24	0.16	0.3	0.14	0.23	0.33	0.23	0.12
MgO	3.55	3.61	3.51	3.98	4	4.3	4.1	3.49	3.64	4.32	4.26	3.92	3.63	4.17	3.94	3.92
CaO	7.66	8.19	9.14	8.58	8.47	8.37	8.51	8.44	6.98	8.66	8.7	8.36	8.8	9.44	8.15	8.26
Na_2O	4.6	4.77	5.14	4.64	5.04	4.69	4.94	4.91	5.22	4.71	4.82	4.67	5.15	4.14	5.36	5.25
K_2O	2.72	3.05	2.96	2.76	2.48	2.58	2.37	2.51	3.44	2.26	2.28	2.41	2.93	1.55	2.32	2.26
P_2O_5	1.14	1.1	0.89	0.9	0.86	0.91	0.95	0.77	0.95	0.83	0.71	0.82	0.89	0.49	0.77	0.66
H_2O	1.54	1.49	0.35	1.45	1.4	1.4	1.44	0.59	1.37	1.68	1.54	1.46	0.48	1.43	1.42	1.42
Cl	0.23	0.23	0.23	0.22	0.25	0.23	0.38	0.23	0.25	0.22	0.2	0.24	0.23	0.29	0.33	0.37
Host Fo	74.1	74.1	74	74.3	74.3	74.3	73.5	73.5	74.2	74.2	74.2	74	73.6	73.6	74.2	74.2
S ppm	129	80	1187	316	1253	420	1467	1285	701	961	1009	684	1055	1704	1773	1619
CO_2	37.3	166	397.4	223.7	450.6	139.2	771	253.7	37.9	705.4	683.4	197.3	263.7	208.4	1228	1010.3
Ba	1053	1076.4	930.3	931.1	909.9	873.1	1025.6	912.1	977.4	822	857.3	851.9	911.2	841.7	853.5	796
Nb	133.5	133.1	84.2	109.7	97.7	104.7	107.7	95.2	111	95.3	95.8	93.7	96.3	98.6	72	70.8
La	136.8	138	105.5	116.4	102.8	105.9	113.9	102.8	107.1	99.2	101.4	103.4	105.9	106	90	90.8
Ce	238.6	238.1	185	207.5	182.7	190	196.6	183.6	186.9	176.6	179.4	179.6	186.7	186.9	167.4	166.7
Sr	788.5	871.9	1121.7	962.1	1115.6	889.1	1468.4	1062.7	709.7	1085.2	1124.2	1049.5	1081	755.2	1615.8	1832.3
Nd	99.5	100.9	77.8	85.5	78.3	79.2	84.4	80.1	74.6	75.1	76.5	77.9	79.6	75.5	81.5	84.3
Sm	15.7	14.4	12.4	14.2	13	12.7	13.8	12.9	11.1	12.4	12.9	12.8	12.6	13.5	14.2	15.9
Zr	429.7	440.1	308.5	376.3	326.8	349.6	344.1	323.3	315.4	326.8	329.3	332.3	335.4	327.3	285.1	303.4
Eu	3.8	3.5	4	3.6	3.4	3.2	3.8	3.4	2.4	2.9	2.9	4	3.6	3.7	4	4.5
Gd	16.1	17.4	13.3	14.7	14.3	13.1	15.2	15	12.2	14.1	13.5	14	12.2	11.6	17.5	14.6
Dy	8.7	9.2	8.4	9.3	8	8.1	10.6	8.5	6.4	8.1	7.7	8.2	9	8.2	9.7	10.2
Y	40.7	42.1	37.2	41.9	36.4	38.3	45.8	35.8	30.6	35.2	36.8	36.6	36.8	32.4	46.2	44
Er	5.2	4.8	4.6	4.8	4.2	4.7	5.1	4.1	4	4.4	4.2	4.1	4.4	3.6	5.1	4.6
Yb	4	4.2	2.7	3.1	3.2	3.1	3.8	2.9	2	2.9	3.7	3.1	3.9	2.7	4.2	4.1
F	1751	1875	2060	1686	2085	1720	2480	1977	1565	1813	1809	1825	1932	1620	1812	1731
Ce/Y	5.9	5.7	5	5	5	5	4.3	5.1	6.1	5	4.9	4.9	5.1	5.8	3.6	3.8
La/Yb	34	32.9	39	37.6	31.9	34.6	29.8	35	53.5	34.6	27.2	33.9	27.2	38.6	21.3	22.2
CO_2/Nb	0.3	1.2	4.7	2	4.6	1.3	7.2	2.7	0.3	7.4	7.1	2.1	2.7	2.1	17.1	14.3
H_2O/Ce	64.5	62.6	18.9	69.9	76.6	73.7	73.2	32.1	73.3	95.1	85.8	81.3	25.7	76.5	84.8	85.2
Sr/Sr*	0.4	0.4	0.7	0.5	0.7	0.5	0.8	0.6	0.4	0.7	0.7	0.6	0.6	0.5	1	1.1

Table S3. Melt inclusions major, trace and volatile element data acquired by EPMA and SIMS with calculated trace element and voaltile ratios, Sr/Sr* and host olivine Fo mol.% for NEMR and SWMR melt inclusions and matrix glasses

MI Name	141a	141b	**SWMR** 6a	6b	6c	41a	46a	46b	50a	50b	50c	50d	57a	67a	109a	**NEMR** 140 MG	**SWMR** 46 MG
SiO_2 wt.%	49.67	48.51	45.33	46.65	47.98	48.32	48.99	50.36	50.73	47.91	48.26	51.3	49.6	48.81	47.45	50.81	51.13
TiO_2	2.06	1.89	1.85	1.8	2.41	1.63	1.52	2.19	1.85	1.51	1.69	1.79	2.1	1.86	1.87	2.27	2.23
Al_2O_3	16.78	16.62	14.77	15.21	15.53	17.22	16.83	17.01	17.14	16.39	15.86	17.66	17.22	16.54	16.55	15.96	16.79
FeO_T	10.62	11.93	12.46	11.77	10.05	11.41	11.46	9.96	9.9	9.8	9.87	9.72	11.03	10.83	10.84	11.07	10.61
MnO	0.19	0.29	0.29	0.19	0.25	0.25	0.23	0.2	0.18	0.19	0.21	0.15	0.25	0.2	0.25	0.24	0.22
MgO	4.17	4.32	4.52	4.26	3.96	4.4	4.21	3.92	3.86	3.71	3.77	3	3.75	4.11	3.62	3.74	3.86
CaO	8.66	9.14	9.99	9.44	7.76	10.4	10.01	8.95	8.25	8.12	8.5	8.61	9.03	9.01	8.68	7.98	8.31
Na_2O	4.72	4.77	4.18	4.41	4.43	4.06	4.82	4.7	4.73	4.57	4.62	4.98	5.21	4.9	4.76	4.72	4.88
K_2O	2.31	1.6	1.19	1.42	2.56	1.22	1.38	2.36	2.69	2.39	2.22	2.68	2.23	1.94	2.25	3.01	2.41
P_2O_5	0.83	0.88	0.53	0.47	0.69	0.27	0.33	0.67	0.61	0.63	0.59	0.61	0.46	0.49	0.49	1.1	0.57
H_2O	1.42	1.32	1.46	1.25	1.4	1.36	1.42	1.46	1.46	1.45	1.42	1.45	1.25	1.46	0.36	0.18	0.25
Cl	0.21	0.31	0.24	0.24	0.26	0.24	0.3	0.19	0.22	0.19	0.16	0.22	0.19	0.21	0.17	0.23	0.19
Host Fo	74.2	74.2	74.2	74.2	75.1	75.4	75.2	75.2	75.1	75.1	75.1	75.1	75.2	75.1	75.1	74.2	75.2
S ppm	1132	1893	1766	1485	196	1556	1674	399	283	524	627	1140	949	973	967	70	150
CO_2	450.3	800.5	686.5	721.2	293.4	637.4	890.6	167.1	198.6	401.1	537	789.3	524.7	592.8	317.5	0	0
Ba	880.2	709.1	582.7	587	1035	489.8	551.4	883.2	932.5	823.3	818.2	934.2	863.7	798.4	828.4	951.5	876.1
Nb	93.9	83.8	74	57.5	125	49.9	53.9	103.2	109.7	93	92.1	98	87	85.7	85.1	113.8	102
La	101.2	91.8	81.7	73	130.4	58	65.4	110.7	115.9	96.4	99.9	108.1	101	95.3	101.5	126.4	108.4
Ce	176.9	173.7	148.3	137.3	225.8	107.2	123.1	198.7	203.3	168.2	172.9	187.8	177	167.7	176.5	219.7	196.2
Sr	1087.4	1353	1082.3	1425.8	784.4	1378.7	1546	911.9	1768.8	883.7	832.6	903.6	1574.6	943.6	1099.8	857.9	997
Nd	73.9	81.2	70.5	69.7	93.2	54.1	61.8	84.9	84.5	68.5	73.8	81.3	77	71.3	72.2	98.9	83
Sm	12.2	14.3	13	12.3	15.2	10.5	13.2	14.3	13.2	11.1	11.9	13	13.2	12.6	12.9	16.2	12.3
Zr	324.6	296.5	303.9	249	415.6	214.4	230	368.4	378.6	312.1	327.8	348.5	323.2	305.9	305.4	414.7	361.1
Eu	2.9	4.7	4	3.7	4.1	3.2	3.8	3.8	3.9	3	3.3	3.8	3.5	3.7	3.5	4.9	4.3
Gd	14.7	17.9	17.2	12.8	13.9	11	15.8	14	16.3	14.1	15.6	14.2	13.8	15.1	15.2	17.4	17.2
Dy	7.6	11.3	10.6	8.2	8.5	7.4	9.9	8.6	8.5	7.9	7.2	7.9	8.6	8.5	8.2	9.7	8.6
Y	35.9	49.5	51.3	44.3	40.4	33.1	48.7	38.5	36.6	35.5	37.9	38.3	36.6	35.1	35.8	45.1	39.9
Er	4.1	5.6	5.4	4.7	4.9	3.1	4.7	3.8	4.4	4.1	4.4	4.2	4.6	4	4.3	5	4.8
Yb	3.8	4.3	5	4.4	4.4	3	3.7	3.9	2.8	3	3.2	3	3.3	3.3	2.9	4.4	1.9
F	1831	2017	2068	1764	1645	1961	2021	1412	1513	1681	1573	1687	1729	1592	1936	1786	1553
Ce/Y	4.9	3.5	2.9	3.1	5.6	3.2	2.5	5.2	5.6	4.7	4.6	4.9	4.8	4.8	4.9	4.9	4.9
La/Yb	26.3	21.3	16.2	16.5	29.8	19.4	17.9	28.2	41.9	31.8	31.3	35.9	30.9	28.7	35.3	28.7	55.7
CO_2/Nb	4.8	9.6	9.3	12.6	2.3	12.8	16.5	1.6	1.8	4.3	5.8	8.1	6	6.9	3.7	0	0
H_2O/Ce	80.3	76	98.4	91	62	126.8	115.4	73.5	71.8	86.2	82.1	77.2	70.6	87	20.4	8.2	12.7
Sr/Sr*	0.7	0.8	0.8	1.1	0.4	1.3	1.3	0.5	1	0.6	0.5	0.5	1	0.6	0.7	0.4	0.6

Table S4. Host olivine major and minor element data acquired by EPMA with calculated Fo mol.% for olivine compositions at the core of each crystal and adjacent to each analysed MI

MI Name	**Location**	**NEMR** 10a	10b	26a	67a	67b	67c	76a	76b	80a	113a	113b	114a	126a	126b	140a	140b
SiO_2 wt.%	adj ol	38.05	38.36	38.37	38.48	38.56	38.52	38.23	38.45	38.52	38.79	38.69	38.54	38.67	38.33	38.51	38.41
TiO_2	adj ol	0	0.02	0.03	0.04	0.04	0.01	0.04	0.04	0.03	0.03	0.04	0.03	0.05	0.02	0.03	0.04
Al_2O_3	adj ol	0.03	0.01	0.03	0.02	0.03	0.01	0.04	0.02	0.03	0.04	0.04	0.03	0.03	0.04	0.04	0.02
FeO_T	adj ol	23.38	23.44	23.4	23.77	23.16	23.76	24.12	23.71	23.97	22.68	23.55	23.46	23.52	24.36	23.47	23.54
MnO	adj ol	0.43	0.45	0.44	0.49	0.46	0.43	0.52	0.4	0.45	0.46	0.47	0.45	0.4	0.49	0.39	0.4
MgO	adj ol	37.69	38.13	38.07	37.87	38.26	38.02	37.35	37.55	37.78	38.15	38.08	38.06	38.26	37.49	37.92	38.17
CaO	adj ol	0.31	0.33	0.3	0.36	0.3	0.35	0.34	0.31	0.3	0.35	0.35	0.32	0.3	0.3	0.33	0.34
Cr_2O_3	adj ol	0	0.03	0	0	0.01	0	0.02	0	0	0.02	0	0	0	0	0	0
P_2O_5	adj ol	0.02	0.02	0.05	0	0.01	0.02	0	0.05	0.02	0.01	0.08	0.01	0.02	0	0.02	0.01
NiO	adj ol	0.03	0.04	0.06	0.04	0.05	0.04	0.02	0.04	0.03	0	0.04	0.02	0.07	0.04	0.07	0.02
Fo mol.%	adj ol	74.2	74.4	74.4	74	74.6	74	73.4	73.8	73.7	75	74.2	74.3	74.4	73.3	74.2	74.3
SiO_2 wt.%	core	38.46	38.46	38.46	38.49	38.49	38.49	38.25	38.25	38.58	38.57	38.57	38.44	38.41	38.41	38.59	38.59
TiO_2	core	0.02	0.02	0.03	0.02	0.02	0.02	0.04	0.04	0.02	0.04	0.04	0.02	0	0	0.01	0.01
Al_2O_3	core	0.03	0.03	0.03	0.04	0.04	0.04	0.03	0.03	0.01	0.02	0.02	0.01	0.02	0.02	0.03	0.03
FeO_T	core	23.79	23.79	23.94	23.31	23.31	23.31	24.29	24.29	23.74	24.17	24.17	23.97	24.35	24.35	23.85	23.85
MnO	core	0.44	0.44	0.46	0.51	0.51	0.51	0.5	0.5	0.46	0.45	0.45	0.46	0.42	0.42	0.43	0.43
MgO	core	37.54	37.54	37.57	38.07	38.07	38.07	37.37	37.37	37.59	37.48	37.48	37.86	37.52	37.52	37.96	37.96
CaO	core	0.31	0.31	0.3	0.35	0.35	0.35	0.35	0.35	0.34	0.33	0.33	0.32	0.3	0.3	0.32	0.32
Cr_2O_3	core	0.01	0.01	0	0.01	0.01	0.01	0	0	0.04	0	0	0	0	0	0	0
P_2O_5	core	0.03	0.03	0.02	0	0	0	0.04	0.04	0.01	0.04	0.04	0.03	0	0	0.04	0.04
NiO	core	0.07	0.07	0.02	0.04	0.04	0.04	0.06	0.06	0.05	0.03	0.03	0.06	0.01	0.01	0.03	0.03
Fo mol.%	core	73.8	73.8	73.7	74.4	74.4	74.4	73.3	73.3	73.8	73.4	73.4	73.8	73.3	73.3	73.9	73.9

MI Name	**Location**	141a	141b	141c	**SWMR** 6a	6b	25a	41a	46a	46b	50a	50b	50c	50d	57a	67a	109a
SiO_2 wt.%	adj ol	38.44	38.5	38.37	37.83	37.74	38.11	37.85	38.02	38.17	38.19	38	38.03	37.98	37.97	38.02	37.32
TiO_2	adj ol	0.02	0	0.04	0.03	0.02	0.03	0.01	0.03	0.03	0.03	0.02	0.04	0.03	0.02	0.06	0
Al_2O_3	adj ol	0.05	0.04	0.05	0.03	0.03	0.02	0.03	0.03	0.03	0.03	0.03	0.03	0.03	0.03	0.03	0.03
FeO_T	adj ol	22.93	24.15	23.82	23.55	23.53	22.5	22.42	22.56	22.49	22.48	22.66	22.51	22.59	22.71	22.09	22.46
MnO	adj ol	0.42	0.45	0.45	0.44	0.43	0.46	0.44	0.39	0.43	0.42	0.42	0.43	0.42	0.46	0.43	0.45
MgO	adj ol	38.49	37.84	37.93	37.81	38.14	38.45	38.65	38.08	38.28	38.3	38.4	37.97	38.4	38.29	38.02	38.53
CaO	adj ol	0.32	0.3	0.31	0.33	0.33	0.29	0.3	0.35	0.31	0.33	0.33	0.31	0.3	0.32	0.34	0.28
Cr_2O_3	adj ol	0	0	0.01	0.01	0.03	0	0	0	0.02	0	0.03	0	0.02	0	0.02	0
P_2O_5	adj ol	0.03	0.01	0.02	0.02	0.02	0.02	0	0	0.02	0	0	0	0.01	0	0.01	0.01
NiO	adj ol	0.07	0.04	0.05	0.09	0.06	0.06	0.04	0.05	0.07	0.06	0.06	0.06	0.04	0.05	0.06	0.02
Fo mol.%	adj ol	74.9	73.6	74	74.1	74.3	75.3	75.4	75.1	75.2	75.2	75.1	75	75.2	75	75.4	75.4
SiO_2 wt.%	core	38.4	n.d.	38.4	37.68	37.68	37.73	38.04	38.12	38.12	37.79	37.79	37.79	37.79	37.86	37.88	37.9
TiO_2	core	0.01	n.d.	0.01	0.02	0.02	0	0	0	0	0.01	0.01	0.01	0.01	0.02	0.02	0.01
Al_2O_3	core	0.02	n.d.	0.02	0.02	0.02	0.04	0.01	0.02	0.02	0.03	0.03	0.03	0.03	0.03	0.03	0.03
FeO_T	core	23.84	n.d.	23.84	23.53	23.53	22.72	22.44	22.33	22.33	22.51	22.51	22.51	22.51	22.38	22.94	22.92
MnO	core	0.48	n.d.	0.48	0.46	0.46	0.39	0.48	0.43	0.43	0.47	0.47	0.47	0.47	0.44	0.47	0.5
MgO	core	37.9	n.d.	37.9	37.79	37.79	38.1	38.28	38.35	38.35	38.28	38.28	38.28	38.28	38.4	38.32	38.22
CaO	core	0.3	n.d.	0.3	0.37	0.37	0.35	0.28	0.32	0.32	0.33	0.33	0.33	0.33	0.25	0.31	0.31
Cr_2O_3	core	0.01	n.d.	0.01	0	0	0	0.02	0	0	0.01	0.01	0.01	0.01	0	0.03	0
P_2O_5	core	0.04	n.d.	0.04	0.03	0.03	0.05	0.01	0.01	0.01	0.02	0.02	0.02	0.02	0.02	0.02	0
NiO	core	0.02	n.d.	0.02	0.04	0.04	0.04	0.03	0.04	0.04	0.05	0.05	0.05	0.05	0.03	0.05	0.05
Fo mol.%	core	73.9	n.d.	73.9	74.1	74.1	74.9	75.3	75.4	75.4	75.2	75.2	75.2	75.2	75.4	74.9	74.8

Table S5. Melt inclusion (MI) Mg# before and after PEC correction, Matrix glass (MG) Mg# and host olivine Fo% = 100*(MgO/X_{MgO}/(MgO/X_{MgO} + FeO/X_{FeO})

Sample name	Mg# MI before PEC	Mg# MI after PEC	Fo% host olivine	Mg# MG
NEMR 114a	41.8	46.3	74.0	n.d
NEMR 26a	38.8	45.6	74.0	40.4
NEMR 140a	41.6	45.8	74.2	40.1
NEMR 140b	41.4	45.7	74.2	40.1
NEMR 113a	44.8	46.8	74.2	n.d.
NEMR 113b	44.8	46.8	74.2	n.d.
NEMR 67a	42.8	47.1	74.4	37.9
NEMR 67b	42.1	46.2	74.3	37.9
NEMR 67c	43.7	46.8	74.3	37.9
NEMR 141a	43.7	46.7	74.2	37.9
NEMR 141b	41.8	47.0	74.2	37.9
NEMR 141c	42.0	45.0	74.2	37.9
NEMR 10a	42.0	46.1	74.1	37.5
NEMR 10b	40.8	46.0	74.1	37.5
NEMR 76a	40.9	45.8	73.5	n.d.
NEMR 76b	38.5	45.2	73.5	39.8
NEMR 126a	38.6	45.1	73.5	40.4
NEMR 126b	41.7	46.6	73.5	40.4
NEMR 80 mg	n.d.	n.d.	73.8	37.9
NEMR 28 mg	n.d.	n.d.	74.1	39.7
SWMR 25a	43.8	47.3	75.1	41.5
SWMR 109a	39.8	47.2	75.1	39.3
SWMR 41a	43.3	48.9	75.3	39.9
SWMR 46a	42.1	48.12	75.2	41.9
SWMR 46b	43.8	47.8	75.2	41.9
SWMR 50a	43.6	47.2	75.1	40.2
SWMR 50b	42.9	47.2	75.1	40.2
SWMR 50c	43.0	47.5	75.1	40.2
SWMR 50d	37.9	47.0	75.1	40.2
SWMR 67a	42.9	51.3	75.1	40.3
SWMR 6a	41.8	47.5	74.2	n.d.
SWMR 6b	41.7	47.2	74.2	n.d.
SWMR 57a	40.2	47.1	75.2	41.3
SWMR 74 mg	n.d.	n.d.	75.0	39.9